TXN, a Xanthohumol Derivative, Significantly Attenuates High-Fat Diet Induced Hepatic Steatosis In Vivo by Antagonizing PPARγ

Yang Zhang[1*], Gerd Bobe[2], Cristobal L. Miranda[3], Malcolm B. Lowry[4], Victor L. Hsu[5], Christiane V. Löhr[6], Carmen P. Wong[1], Donald B. Jump[1], Matthew M. Robinson[7], Thomas J. Sharpton[8], Claudia S. Maier[9], Jan F. Stevens[3], Adrian F. Gombart[10*]

[1]School of Biological and Population Health Sciences, Nutrition Program, Linus Pauling Institute, Oregon State University, Corvallis, OR 97331, USA

[2]Department of Animal Sciences, Linus Pauling Institute, Oregon State University, Corvallis, OR 97331, USA

[3]Department of Pharmaceutical Sciences, Linus Pauling Institute, Oregon State University, Corvallis, OR 97331, USA

[4]Department of Microbiology, Oregon State University, Corvallis, OR 97331, USA

[5]Department of Biochemistry and Biophysics, Oregon State University, Corvallis, OR 97331, USA

[6]Department of Biomedical Science, Carlson College of Veterinary Medicine, Corvallis, OR 97331, USA

[7]School of Biological and Population Health Sciences, Kinesiology Program, Oregon State University, Corvallis, OR 97331, USA

[8]Department of Microbiology, Department of Statistics, Oregon State University, Corvallis, OR 97331, USA

[9]Department of Chemistry, Linus Pauling Institute, Oregon State University, Corvallis, OR 97331, USA

[10]Linus Pauling Institute, Department of Biochemistry and Biophysics, Oregon State University, Corvallis, OR 97331, USA

[*]Authors to whom correspondence should be addressed.

Abstract

We previously reported xanthohumol (XN), and its synthetic derivative tetrahydro-XN (TXN) attenuates high-fat diet (HFD) induced obesity and metabolic syndrome in C57BL/6J mice. The objective of the current study was to determine the effect of XN and TXN on lipid accumulation in the liver. Non-supplemented mice were unable to adapt their caloric intake to 60% HFD, resulting in obesity and hepatic steatosis; however, TXN reduced weight gain and decreased hepatic steatosis. Liver transcriptomics indicated TXN might antagonize lipogenic PPARγ actions *in vivo*. XN and TXN inhibited rosiglitazone-induced 3T3-L1 cell differentiation concomitant with decreased expression of lipogenesis-related genes. A PPARγ competitive binding assay showed XN and TXN bind to PPARγ with an IC_{50} similar to pioglitazone and 8-10 times stronger than oleate. Molecular docking simulations demonstrated XN and TXN bind in the PPARγ ligand-binding domain pocket. Our findings are consistent with XN and TXN acting as antagonists of PPARγ.

Introduction

Non-alcoholic fatty liver disease (NAFLD) is a major global health threat characterized by excessive hepatic lipid droplet accumulation with a history of little or no alcohol consumption (Hashimoto, Taniai and Tokushige, 2013). About one-quarter of the US population suffers from NAFLD (Estes *et al.*, 2018) with rates in the rest of the world ranging from 14% in Africa to 32% in the Middle East (Younossi *et al.*, 2016). The continuing obesity and diabetes epidemic drives increasing rates of NAFLD (Estes *et al.*, 2018). Unfortunately, no FDA-approved drugs exist for its treatment. Sustained healthy life style changes and weight loss are the only interventions proven effective in preventing the onset and progression of NAFLD (Stefan, Häring and Cusi, 2019). Thus, there is a critical need for novel and effective interventions.

As a central hub for lipid metabolism, a healthy liver maintains homeostasis among uptake, esterification, oxidation and secretion of fatty acids (FAs) (Goldberg and Ginsberg, 2006). Overconsumption of saturated FAs or sugars can overload the liver, disrupt lipid homeostasis, resulting in excess storage of triacylglycerols (TAG) in hepatocytes and the onset and progression of hepatic steatosis (Ipsen, Lykkesfeldt and Tveden-Nyborg, 2018). Given that PPARγ is important in hepatic lipogenesis (Sharma and Staels, 2007), it has attracted

55 considerable attention as a therapeutic target for NAFLD (Almeda-Valdés, Cuevas-Ramos and
56 Aguilar-Salinas, 2009).

57 Attenuated PPARγ activity in heterozygous PPARγ-deficient (*PPARγ*$^{+/-}$) C57BL/6J mice
58 protects against HFD-induced obesity, liver steatosis and adipocyte hypertrophy; however,
59 treatment with the PPARγ agonist pioglitazone (PGZ) abrogates the protection against
60 hypertrophy and decreases insulin sensitivity (Kubota *et al.*, 1999) suggesting a potential
61 beneficial use for PPARγ antagonists to treat hepatic steatosis. PPARγ antagonists tanshinone
62 IIA (Gong *et al.*, 2009), β-cryptoxanthine (Goto *et al.*, 2013), protopanaxatriol (Zhang *et al.*,
63 2014), isorhamnetin (Zhang *et al.*, 2016), and Gleevec (Choi *et al.*, 2016) improved multiple
64 metabolic parameters in diet-induced obese (DIO) mice. These observations strongly suggest that
65 moderate inhibition of PPARγ activity may reduce the risk for developing hepatic steatosis
66 induced by diet, and PPARγ antagonists may be useful for the treatment and prevention of
67 NAFLD.

68 Xanthohumol (XN), a prenylated flavonoid found in hops (*Humulus lupulus* L.),
69 improves multiple parameters of MetS in rat and mouse models (Legette *et al.*, 2014; Miranda *et*
70 *al.*, 2016, 2018). Tetrahydroxanthohumol (TXN), a non-estrogenic synthetic XN derivative (**Fig.**
71 **1**), appears more effective in ameliorating MetS in DIO mice than XN possibly due to its 5-, 10-,
72 and 12-fold higher levels in the muscle, plasma and liver, respectively, as compared with XN
73 (Miranda *et al.*, 2018). Both compounds likely mediate their benefits via multiple mechanisms.
74 XN inhibits differentiation of preadipocytes and induces apoptosis in mature adipocytes (Yang *et*
75 *al.*, 2007; Rayalam *et al.*, 2009), attenuates the function of SREBP-1 by repressing its maturation
76 (Miyata *et al.*, 2015) and induces beiging of white adipose tissue, decreases adipogenesis, and
77 induces lipolysis (Samuels, Shashidharamurthy and Rayalam, 2018). We recently showed that
78 XN and TXN significantly change gut microbiota diversity and abundance, alter bile acid
79 metabolism and reduce inflammation in mice fed a HFD (Zhang *et al.*, 2020). Collectively, these
80 data suggest both XN and TXN are effective for treatment of metabolic disorders and are
81 promising candidates for NAFLD prevention and treatment.

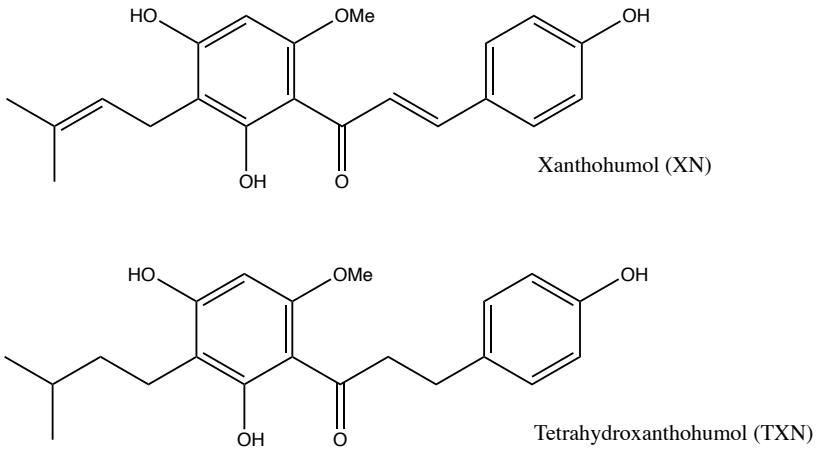

Figure 1. Structures of XN and its synthetic derivative TXN.

In the present study, we show a daily oral intake of TXN at 30 mg/kg body weight (BW) or XN at a daily dose of 60 mg/kg BW strongly suppresses diet-induced liver steatosis in C57BL/6J male mice. Supervised machine learning of liver RNA-seq data identified perturbations in PPARγ signaling. Based on cell culture experiments, a PPARγ competitive binding assay and molecular docking studies, we provide evidence that XN and TXN act as novel PPARγ antagonists with moderate binding activity. Collectively, our findings suggest appropriate functional antagonism of PPARγ is a logical approach to prevent and treat diet-induced liver steatosis and other related metabolic disorders. The structures of XN and TXN could serve as scaffolds for synthesis of more effective compounds to treat NAFLD.

Results

1. TXN attenuates HFD-induced weight gain independent of caloric intake

As expected, C57BL/6J mice on a 60% HFD (**Fig. S1A**, solid blue line) gained more BW than mice on the LFD (**Fig. S1A**, dotted black line) throughout the experimental period (week 1: $p < 0.05$; week 2-16: $p < 0.001$; repeated measures). TXN-supplementation (**Fig. S1A**, solid dark green line) attenuated HFD-induced BW gain throughout the experimental period (week 1: $p < 0.05$; week 2-16: $p < 0.001$; repeated measures). XN supplementation showed a dose response effect: the higher dosage (HXN; **Fig. S1A**, solid red line), but not the lower dosage (LXN; **Fig. S1A**, solid yellow line), attenuated HFD-induced BW gain between week 8 and 16. When BW gain was expressed as % of initial BW, HFD-fed mice almost doubled their initial BW (+98.3 ± 2.7%), whereas TXN-treated mice gained 33% less (+66.2 ± 5.8%, $p < 0.0001$), and LFD-fed

104 mice gained 53% less (+45.8 ± 4.3%, $p < 0.0001$) than HFD-fed mice (**Fig. S1B**). Although not
105 statistically significant, both LXN- and HXN-treated mice gained 7.5% and 11% less,
106 respectively (90.0 ± 3.3%, $p = 0.20$; 87.6 ± 3.9%, $p = 0.07$; **Fig. S1B**). In male C57BL/6J mice, a
107 BW of approximately 40 g is a critical tipping point from whereon metabolic dysfunction occurs
108 (van Beek *et al.*, 2015). After 16 weeks, mean BW for these mice was LFD (37.5 ± 1.1g), HFD
109 (50.3 ± 0.6g), LXN (49.9 ± 1.1g), HXN (47.4 ± 1.1g) and TXN (42.2 ± 1.6g).

110 Overtime, mice adapted to the HFD by consuming less food than LFD-fed mice (**Fig.**
111 **S1C**). However, the discrepancy in food consumption was insufficient to counteract the elevated
112 caloric intake (**Fig. S1D**). HXN-treated mice adapted better to the HFD, indicated by decreased
113 food intake at week 1, 6-10, 13, and 16 ($p < 0.05$), and caloric intake ($p = 0.01$) (**Fig. S1C-D**),
114 resulting in less BW gain. In contrast, the attenuated BW gain in TXN-treated mice was not
115 accompanied by a significant reduction in food or caloric intake (**Fig. S1C-D**).

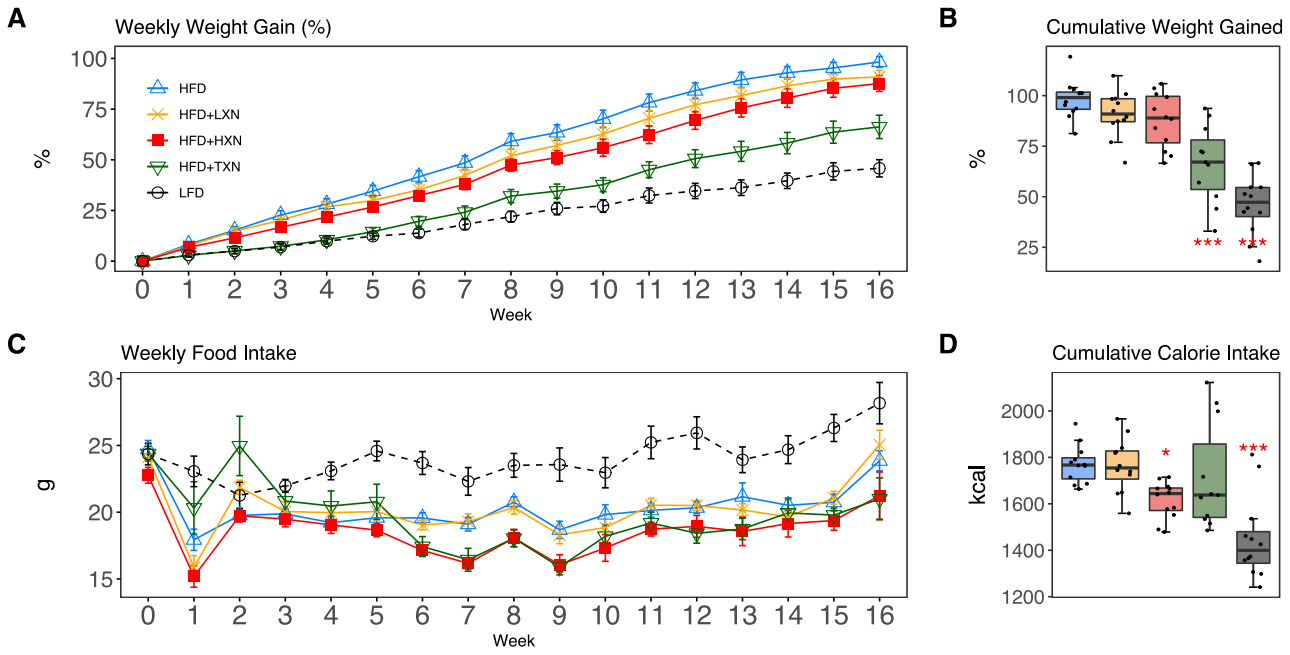

Figure S 1. TXN and HXN suppress HFD-induced BW gain independent of caloric intake. Mice were fed either a LFD (black dashed line with empty circles, n = 12), a HFD (blue solid line with empty triangles, n = 12), HFD+LXN (yellow solid line with crosses, n = 12), HFD+HXN (red solid line with squares, n = 12), or HFD+TXN (green solid line with empty triangles, n = 11) for 16 weeks. (A) BW gain was assessed once per week. Data is expressed as means ± SEM. Repeated measurement of ANOVA was used to calculate *p*-values for the percentage of weight gained weekly. (B) Total percent BW gained at the end of the16-week feeding period. Data is expressed as quartiles. (C) Food intake was assessed once per week during the 16-week feeding period. Data is expressed as means ± SEM. Repeated measurement of ANOVA was used to calculate *p*-values for weekly food intake. (D) Total calories consumed at the end of 16-week feeding period. Data are expressed as quartiles.

127 **2. TXN attenuates hepatic steatosis and HFD-induced obesity**

128 HFD-induced BW gain was primarily body fat accumulation, as indicated by measurements
129 obtained from DEXA scans. HFD mice had greater fat mass than LFD mice ($p < 0.0001$; **Fig.**
130 **2A**). Linear regression of total fat mass to total caloric intake revealed a strong relationship
131 between caloric intake and fat mass among groups (r = +0.52; $p < 0.0001$) and within LFD-fed
132 mice (r = +0.79; $p = 0.002$; **Fig. 2A1**). In contrast, caloric intake was not correlated to fat mass in
133 any HFD group (**Fig. 2A2-5**), indicating a disconnection between caloric intake and fat mass
134 after prolonged HFD consumption. Supplementation with HXN (-9.93%; $p < 0.05$) and even
135 more so with TXN (-27.7%; $p < 0.001$) decreased body fat mass on HFD (**Fig. 2A**), indicating
136 that HXN and TXN attenuated the HFD-induced body fat accumulation and that this effect was
137 not explained by changes to caloric intake (**Fig. 2A4-5**).

138 Hepatic steatosis was measured by percent surface area occupied by lipid vacuoles in
139 formalin-fixed, paraffin-embedded liver by image analysis of photomicrographs. In the absence
140 of supplementation, HFD- and LFD-fed mice shared similar hepatic lipid areas (**Fig. 2B**). Caloric
141 intake was positively correlated with hepatic lipid area on both LFD-fed mice (r = +0.61, $p =$
142 0.03; **Fig. 2B1**) and a HFD (r = +0.57, $p = 0.05$; **Fig. 2B2**). Supplementation with HXN ($p <$
143 0.05) and TXN ($p < 0.01$) mitigated hepatic steatosis, independent of caloric intake (**Fig. 2B4-5**).

144 Changes in energy balance may drive changes in obesity-related steatosis. We
145 investigated TXN on whole-body energy metabolism to determine mechanisms of TXN
146 protection from weight gain, which can influence steatosis. Towards the end of the study, we
147 measured whole-body expenditure for all 59 mice using a computer-controlled indirect
148 calorimetry system (metabolic cages). Energy expenditure was calculated from the oxygen and
149 carbon dioxide exchange ratio using the Weir equation (Weir, 1949). Total energy expenditure
150 contains energy expenditure for basal metabolism, body tissue synthesis, digestion, and physical
151 activity (Speakman, 2013). Mice consuming HFD and mice supplemented with LXN had higher
152 ($p < 0.05$) energy expenditure than mice on LFD, HXN and TXN (**Fig. 2C**). Caloric intake was
153 positively correlated with energy expenditure in LFD- (**Fig. 2C1**), LXN- (**Fig. 2C3**), HXN- (**Fig.**
154 **2C4**) and TXN-fed mice (**Fig. 2C5**) but was not correlated with energy expenditure in HFD mice
155 (**Fig. 2C2**). We investigated the influence of body mass on energy expenditure using analysis of
156 covariance (ANCOVA) of body mass upon entry into the cages between diets (Tschöp *et al.*,

157 2011). ANCOVA revealed that LXN, HXN, or TXN supplementation did not change the positive
158 relationship between energy expenditure and body mass (**Figure S2**).

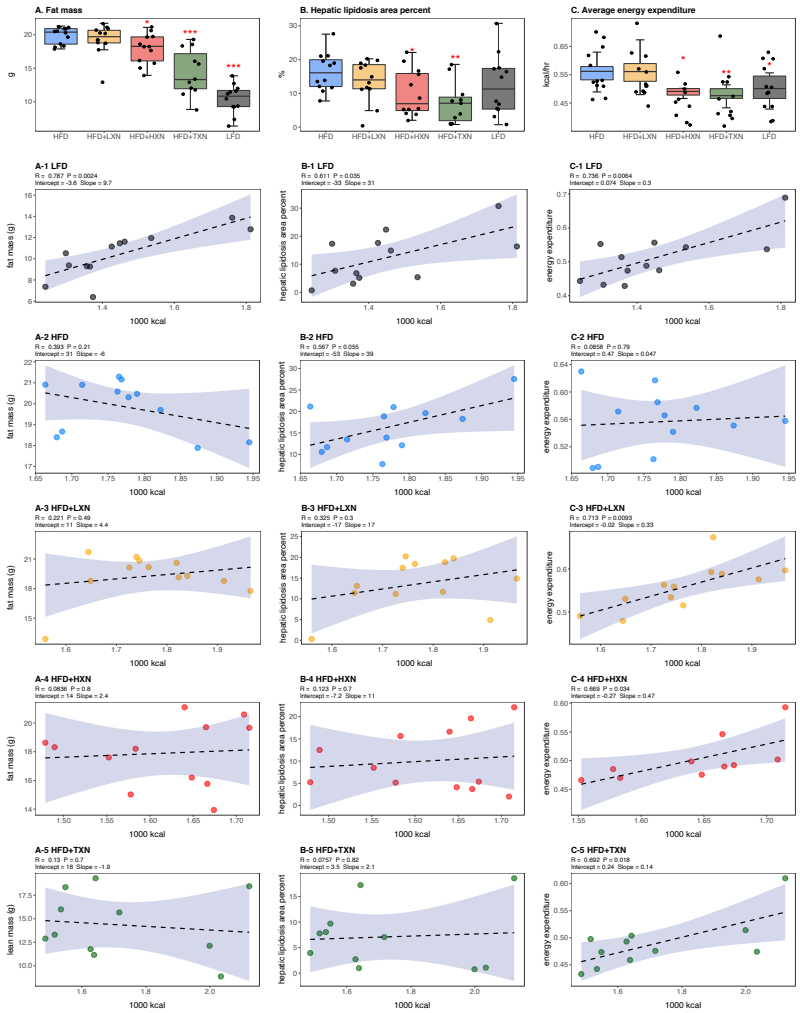

Figure 2. Energy homeostasis imbalance induced by HFD is prevented by XN and TXN supplementation. Mice were fed either a LFD (black, n = 12), a HFD (blue, n = 12), HFD+LXN (yellow, n = 12), HFD+HXN (red, n = 12), or HFD+TXN (green, n = 11) for 16 weeks. (A) Total fat mass measured by DXA scan two days prior to necropsy is expressed as quartiles. (A-1) Relationship between total fat mass and total caloric intake over 16 weeks of feeding for LFD; (A-2) HFD; (A-3) HFD+LXN; (A-4) HFD+HXN; and (A-5) HFD+TXN groups. (B) Hepatic lipidosis area percent expressed as quartiles. (B-1) Relationship between hepatic lipidosis area percent and total caloric intake over 16 weeks of feeding for LFD; (B-2) HFD; (B-3) HFD+LXN; (B-4) HFD+HXN; and (B-5) HFD+TXN groups. (C) Average energy expenditure over two light-dark cycles (48 hours) obtained using metabolic cages and expressed as quartiles. (C-1) Relationship between energy expenditure and total caloric intake over 16 weeks of feeding for LFD; (C-2) HFD; (C-3) HFD+LXN; (C-4) HFD+HXN (with removal of two outliers); (C-5) for HFD+TXN groups. Pre-planned general linear model with contrasts were used to calculate *p*-values in A, B and C. $*p < 0.05$, $**p < 0.01$, $***p < 0.001$. Linear regression analyses of total calories versus total fat mass (A1-5), hepatic lipidosis area percent (B1-5), and average energy expenditure (C1-5) in mice were done using stats package version 3.6.2 in R. Blue shading represents 95% CI of the regression line. Absolute value of R, p-value, intercept, and slope for the regression are reported above each corresponding panel.

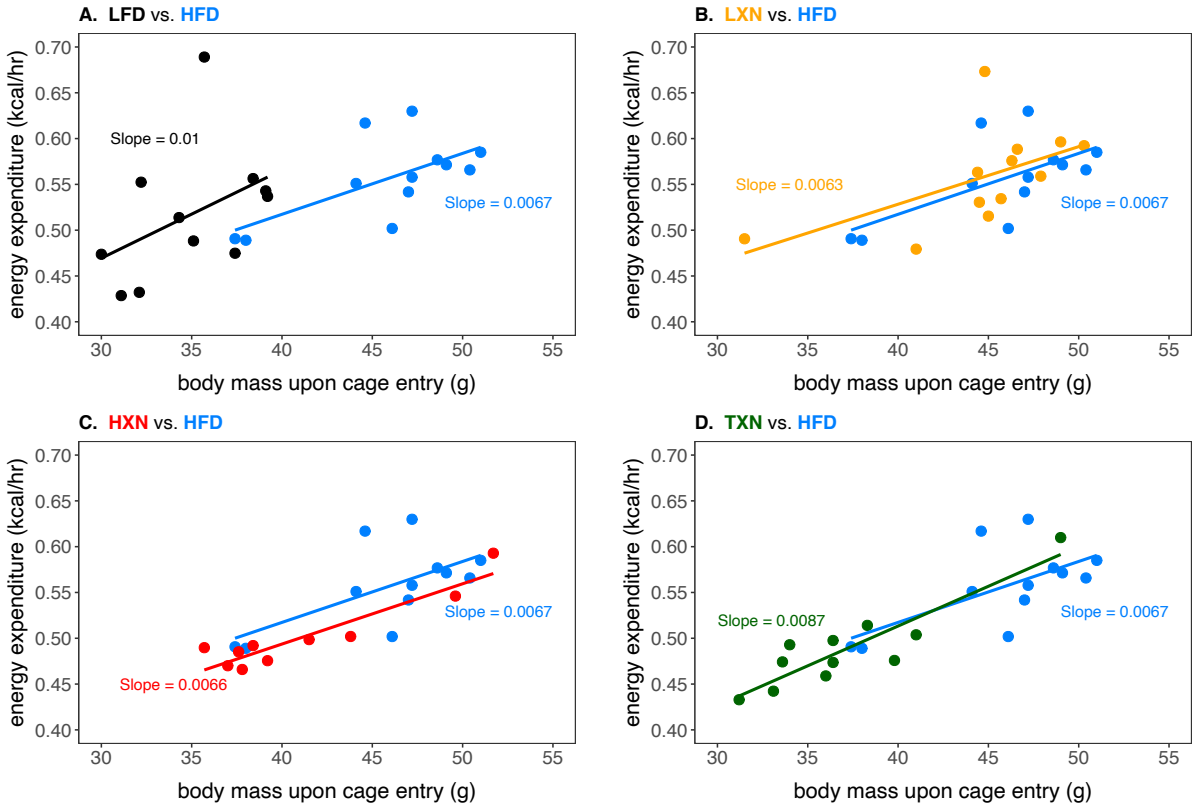

Figure S 2. Relationship of body mass and energy expenditure between (A) LFD and HFD; (B) LXN and HFD; (C) HXN and HFD; (D) TXN and HFD. Energy expenditure was measured between weeks 10 to 14. Data was analyzed using analysis of covariance (ANCOVA) of body mass upon entry into the cages and diet. No statistically significant effect from treatments was detected. HFD data are from the same group of mice and are displayed as a reference on all four panels.

As a marker of hepatic lipid uptake and export, fasting plasma TAG level was measured at the end of the study. Similar to hepatic lipid area, fasting plasma TAG did not reflect the caloric density of the diet (**Fig. S3A**); namely, there was an inverse relationship between caloric intake and plasma TAG among LFD mice (Spearman, r = -0.60, $p = 0.04$; **Fig. S3A1**), which was lost on the HFD (**Fig. S3A2**). TXN treatment restored the negative correlation between caloric intake and plasma TAG (Spearman r = -0.65, $p = 0.04$). One explanation for the higher plasma TAG ($p < 0.01$) observed could be that TXN inhibited hepatic lipid uptake, and promoted hepatic lipid export, or both. TAG levels remained in the normal physiological range (40 to 60 mg/dL) for all groups (Bogue *et al.*, 2020).

We collected fecal pellets over a 3-day period and measured fecal TAG at the end of the study as an indicator of fecal energy excretion. Fecal TAG levels did not differ among all groups (**Fig. S3B**). No relationship was observed between caloric intake and fecal TAG among or within

groups (**Fig. S3B1-5**), suggesting that the attenuated BW gain and hepatic steatosis in TXN- and HXN-treated mice was not related to increased fecal TAG excretion.

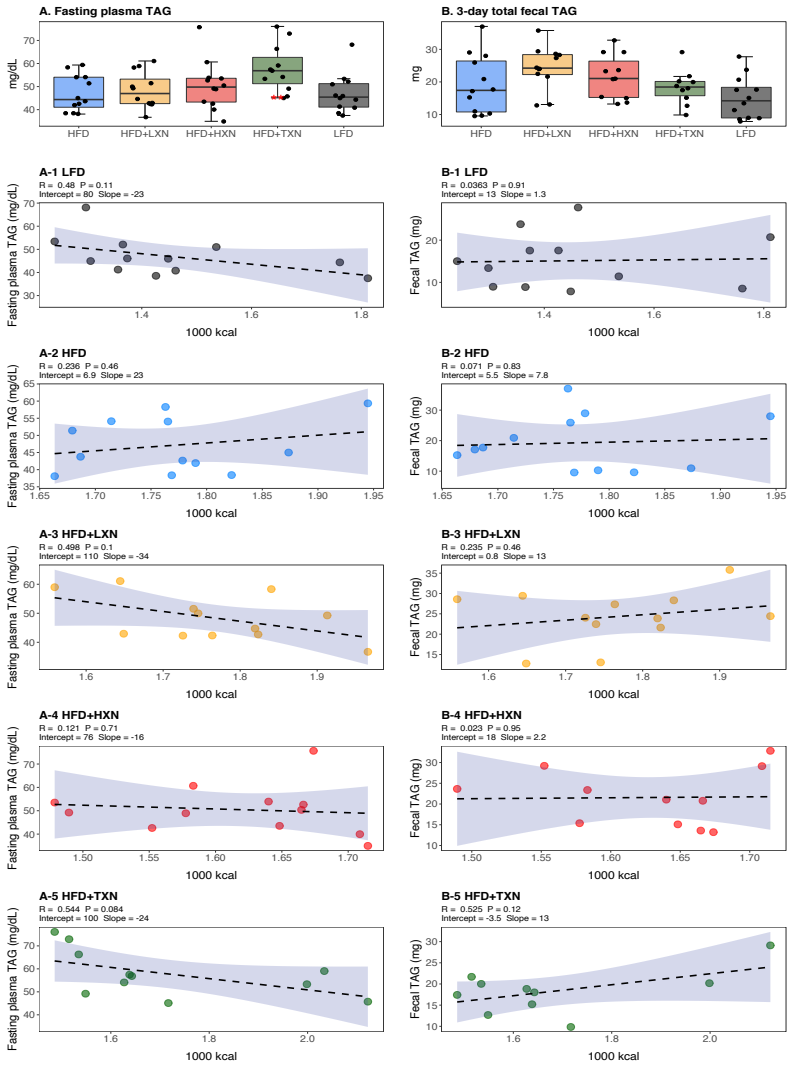

Figure S 3. The effect of diet and intervention on fasting plasma and fecal TAG levels. Mice were fed either a LFD (black, n = 12), a HFD (blue, n = 12), HFD+LXN (yellow, n = 12), HFD+HXN (red, n = 12), or HFD+TXN (green, n = 11) for 16 weeks. (A) Fasting plasma TAG levels are expressed as quartiles. (A-1) Relationship between fasting plasma TAG and total caloric intake over 16 weeks of feeding for LFD group; (A-2) for HFD group; (A-3) for HFD+LXN group; (A-4) for HFD+HXN group; (A-5) for HFD+TXN group (B) 3-day total fecal triglyceride (TAG) are expressed as quartiles. (B-1) Relationship between 3-day fecal TAG and total caloric intake over 16 weeks of feeding for LFD group; (B-2) for HFD group; (B-3) for HFD+LXN group; (B-4) for HFD+HXN group; (B-5) for HFD+TXN group. Pre-planned general linear model with contrasts were used to calculate *p*-values in A, B and C. **p* < 0.05, ***p* < 0.01, ****p* < 0.001. Linear regression analyses of total calories versus fasting plasma TAG (A1-5) or total fecal TAG (B1-5) in mice were done using lm function of stats package version 3.6.2 in R. Blue shading represents 95% CI of the regression line. Absolute value of R, p-value, intercept, and slope for the regression are reported above each corresponding panel.

211 **3. Effects of XN and TXN on food intake frequency, physical activity and energy**
212 **expenditure**

213 We considered if physical activity level could explain attenuated weight gain of XN- and TXN-
214 treated groups. We differentiated activity measured in the metabolic cages into directed
215 ambulatory locomotion (sum of all locomotion of 1 cm/second or above within the x, y beam-
216 break system) (**Fig. 3A**) and fine movements (e.g., grooming, nesting and scratching) (**Fig. 3B**).
217 In addition, we approximated the ambulatory movement for food consumption by measuring
218 feeding frequency (**Fig. 3C**). In contrast to energy expenditure (**Fig. 2C**), directed ambulatory
219 locomotion was lower in HFD- than LFD-fed mice (**Fig. 3A**), while fine movement level (**Fig.**
220 **3B**) and feeding frequency (**Fig. 3C**) were not changed. TXN-treated mice exhibited higher
221 directed ambulatory locomotion and fine movement levels than HFD mice (**Fig. 3A, B**), whereas
222 feeding frequency was unchanged (**Fig. 3C**). XN-treated HFD mice showed higher directed
223 ambulatory locomotion activity and feeding frequency than HFD mice (**Fig. 3A, C**), whereas
224 fine movement activity levels were not affected (**Fig. 3B**).

225 In HFD-fed and LXN-treated mice, directed ambulatory locomotion levels were
226 positively correlated with food frequency (**Fig. 3C2-3**) but negatively correlated with energy
227 expenditure (**Fig. 3A2-3**), suggesting that food-driven activity may account for a major part of
228 total directed ambulatory motion and that these mice spent the majority of their time and energy
229 moving around for food consumption. In summary, HFD-fed mice used more energy for
230 maintaining basal metabolism, body tissue turnover, or digestion as indicated by a higher energy
231 expenditure and lower directed ambulatory locomotion activity than LFD mice. Compared to
232 HFD only mice, XN- and TXN-treated mice had lower energy expenditure and higher directed
233 ambulatory locomotion and fine movement activities, indicating lower energy for maintaining
234 basal metabolism, body tissue turnover, or digestion and remained more physically active than
235 untreated HFD-fed mice.

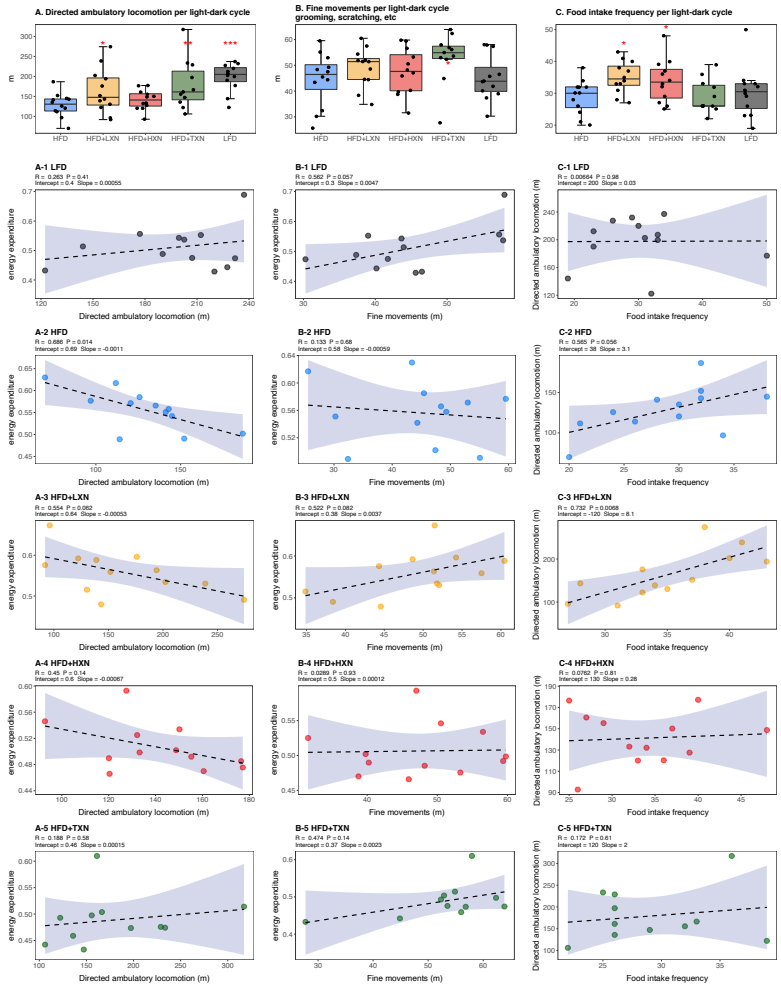

Figure 3. Effects of XN and TXN on food intake frequency, physical activity and energy expenditure. Mice were fed either a LFD (black, n = 12), a HFD (blue, n = 12), HFD+LXN (yellow, n = 12), HFD+HXN (red, n = 12), or HFD+TXN (green, n = 11) for 16 weeks. (A) Directed ambulatory locomotion per 24-hour cycle obtained using a computer controlled indirect calorimetry system. Data expressed as quartiles. (A-1) Relationship between directed ambulatory locomotion and energy expenditure for LFD; (A-2) HFD; (A-3) HFD+LXN; (A-4) HFD+HXN and (A-5) HFD+TXN groups. (B) Fine movements per 24-hour cycle calculated by subtracting directed ambulatory locomotion from sum of all distances traveled within the beam-break system. Data is expressed as quartiles. (B-1) Relationship between fine movements and energy expenditure for LFD; (B-2) HFD; (B-3) HFD+LXN; (B-4) HFD+HXN; and (B-5) HFD+TXN groups. (C) Number of food intake events recorded in metabolic cages. Data expressed as quartiles. (C-1) Relationship between number of food intake events and directed ambulatory locomotion for LFD; (C-2) HFD; (C-3) HFD+LXN; (C-4) HFD+HXN; (C-5) for HFD+TXN groups. Pre-planned general linear model with contrasts were used to calculate *p*-values in A, B and C. *$p < 0.05$, **$p < 0.01$, ***$p < 0.001$. Linear regression analyses of energy expenditure versus directed ambulatory locomotion (A1-5), fine movements (B1-5), and directed ambulatory locomotion and number of food intake events (C1-5) in mice were done using stats package version 3.6.2 in R. Blue shading represents 95% CI of the regression line. Absolute value of R, p-value, intercept, and slope for the regression are reported above each corresponding panel.

255 **4. TXN attenuates HFD-induced lipid accumulation in white adipose tissue (WAT)**

256 To assess the effect of XN and TXN on lipid accumulation, fat pads from three distinct sites:
257 subcutaneous (sWAT), epididymal (eWAT), and mesenteric (mWAT) adipose tissue were
258 carefully removed and weighed during necropsy. Diet-induced lipid accumulation differed by
259 adipose site. Compared to the LFD, the HFD-induced increase in mWAT fat mass was much
260 greater than the increase in sWAT fat mass (three-fold vs. 2.5-fold increase, respectively), with
261 the smallest increase (15%) observed in eWAT fat mass (**Fig. 4A, C**). Supplementation with
262 HXN ($p < 0.05$), and even more so TXN ($p < 0.0001$), decreased sWAT and mWAT fat mass. A
263 smaller but significant increase in eWAT adipose tissue weight was observed in HXN- and
264 TXN-treated mice (**Fig. 4B**).

265 Caloric intake across diets was positively correlated with sWAT (r = +0.47; $p = 0.0002$;
266 **Fig. 4A**) and mWAT fat mass (r = +0.39; $p = 0.002$; **Fig. 4C**), but no relationship was observed
267 within XN- or TXN-treated groups (**Fig. 4A3-5, C3-5**), indicating lipid accumulation in sWAT
268 and mWAT fat depots was primarily linked to diet rather than the amount of food consumed. In
269 eWAT adipose depot, we observed the opposite. Unlike sWAT and mWAT fat depots, caloric
270 intake across diets was not correlated with eWAT fat mass (r = +0.03; $p = 0.82$; **Fig. 4B**).
271 Instead, a positive correlation between caloric intake and eWAT fat mass was found within LFD-
272 fed mice (**Fig. 4B1**), and a negative correlation between caloric intake and eWAT fat mass was
273 observed in both XN- and TXN-treated mice (**Fig. 4B3-5**). No correlation was found in HFD-fed
274 control mice (**Fig. 4B2**). These observations are consistent with distinct WAT depots in mice
275 differing in expandability (van Beek *et al.*, 2015).

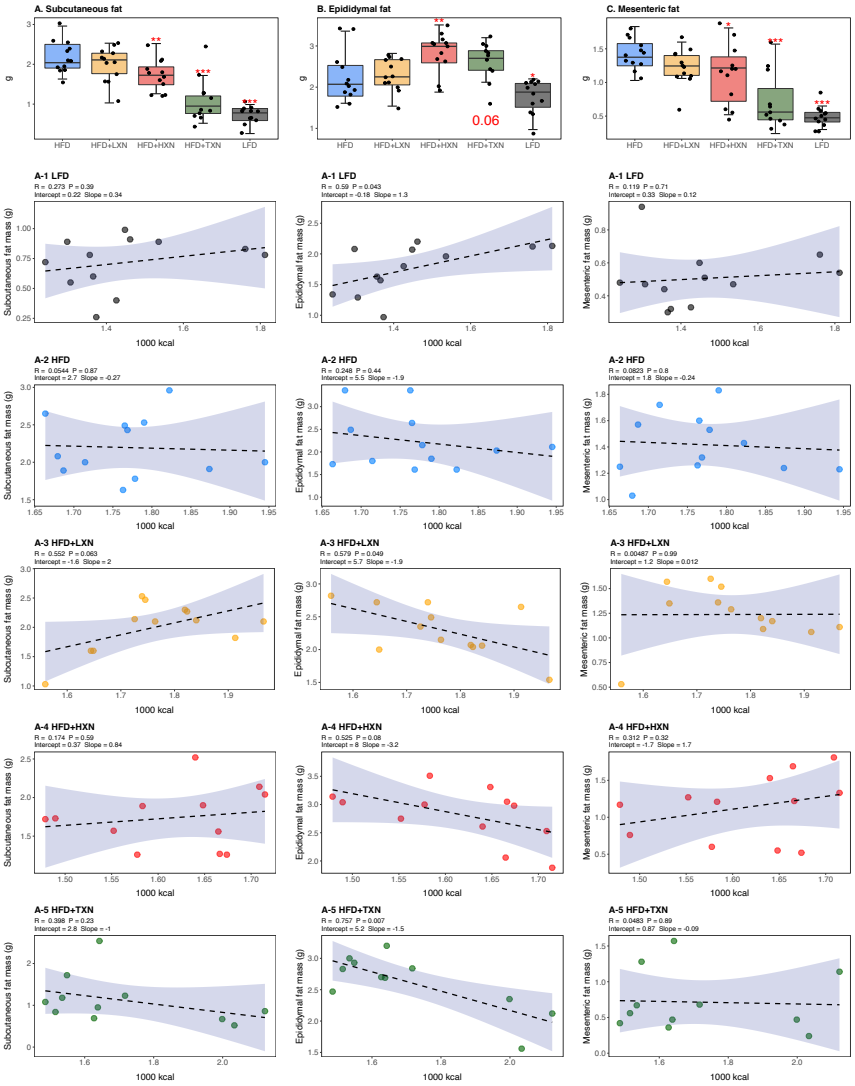

Figure 4. TXN decreases and alters the regional distribution of fat tissue accumulation. Mice were fed either a LFD (black, n = 12), a HFD (blue, n = 12), HFD+LXN (yellow, n = 12), HFD+HXN (red, n = 12), or HFD+TXN (green, n = 11) for 16 weeks. All fat masses were weighed on day of necropsy. (A) sWAT fat mass expressed as quartiles. (A-1) Relationship between sWAT fat mass and total caloric intake over 16 weeks of feeding for LFD; (A-2) HFD; (A-3) HFD+LXN; (A-4) HFD+HXN; and (A-5) HFD+TXN groups. (B) eWAT fat mass expressed as quartiles. (B-1) Relationship between eWAT fat mass and total caloric intake over 16 weeks of feeding for LFD; (B-2) HFD; (B-3) HFD+LXN; (B-4) HFD+HXN; and (B-5) HFD+TXN groups. (C) mWAT fat mass expressed as quartiles. (C-1) Relationship between mWAT fat mass and total caloric intake over 16 weeks of feeding for LFD; (C-2) HFD; (C-3) HFD+LXN; (C-4) HFD+HXN (with removal of two outliers); (C-5) and for HFD+TXN groups. Pre-planned general linear model with contrasts were used to calculate *p*-values in A, B and C. *$p < 0.05$, **$p < 0.01$, ***$p < 0.001$. Linear regression analyses of total calories versus sWAT (A1-5), eWAT (B1-5), and mWAT fat masses (C1-5) in mice were done using stats package version 3.6.2 in R. Blue shading represents 95% CI of the regression line. Absolute value of R, p-value, intercept, and slope for the regression are reported above each corresponding panel.

292 **5. HXN and TXN protect against NAFLD on a high-fat diet**

293 NAFLD is characterized by accumulation of number and size of intrahepatic microvesicular and
294 macrovesicular lipid vacuoles. Mice on a LFD diet possessed hepatic lipid vacuoles and
295 resembled livers of $LDLR^{-/-}$ mice on a similar synthetic diet (Lytle and Jump, 2016); however
296 their liver to BW ratio of about 4% was in a normal healthy range (Lytle, Wong and Jump,
297 2017). HFD fed mice had many smaller lipid vacuoles (**Fig. 5A**). Supplementation with XN
298 decreased in a dose-dependent manner the number and size of intrahepatic lipid vacuoles in HFD
299 mice. Supplementation with TXN almost completely prevented hepatic lipid vacuole
300 accumulation in HFD mice, resulting in less lipid accumulation than in LFD mice.

301 The liver to BW ratio is an indicator of NAFLD with a ratio above 4% indicating
302 NAFLD (Lytle, Wong and Jump, 2017). The majority of mice (10 of 12) on a HFD diet had a
303 liver to BW ratio above 4.5%, whereas all LFD mice had a liver to BW ratio between 3.8 and
304 4.3% (**Fig. 5B**). Supplementation with HXN decreased the number of mice with a liver to BW
305 ratio above 4% to four of 12 mice and all TXN-supplemented mice had a liver to BW ratio below
306 3.6% except for one, which had a liver to BW ratio of 4%. These data are consistent with TXN
307 and, to a smaller extent, HXN reducing NAFLD. Hepatic lipid extracts from TXN-supplemented
308 HFD mice and LFD-fed mice had lower liver triglyceride concentrations than from mice fed with
309 HFD, LXN or HXN (**Fig. 5C**).

310 Another indicator of NAFLD is the liver area occupied by lipids; the histological lower
311 cut-off for NAFLD is over 5% of liver area (Brunt and Tiniakos, 2010). Using this cut-off, all
312 control HFD mice had NAFLD and 10 out of 12 LFD mice had NAFLD (**Fig. 2B**). Both HXN-
313 and TXN supplementation decreased liver lipid accumulation on a HFD by two-fold, as three out
314 of 12 HXN-supplemented mice and five out of 11 TXN-supplemented mice had less than 5%
315 lipid area and nine out of 11 TXN-supplemented mice had less than 10% lipid area (**Fig. 2B**). In
316 comparison, only one out of 12 HFD control mice and seven out of 12 HXN-supplemented mice
317 were below 10% lipid area. The supplement-induced decrease was independent of caloric intake
318 (**Fig 2. B3-5**).

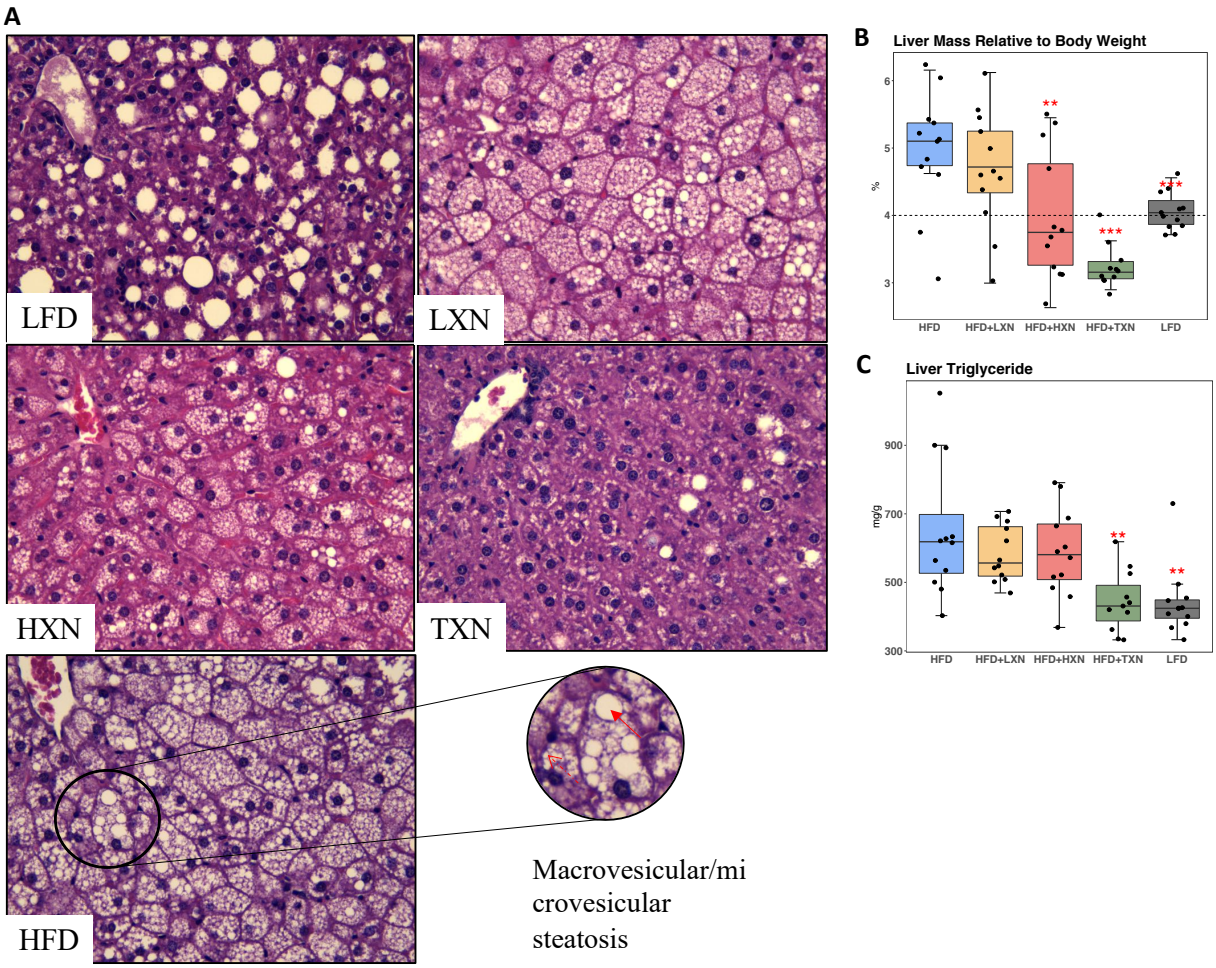

Figure 5. TXN prevents HFD induced liver steatosis in mice. Mice were sacrificed at the end of the study and liver samples were freshly collected and processed. (A) Representative histological images of H&E staining of liver sections. An enlarged image representative of a liver section from a HFD fed mouse is shown as a circle on the bottom right. Macrovesicular steatosis or large lipid droplets are indicated by the red bold arrow; microvesicular steatosis or small lipid droplets are indicated by the broken red line arrow. (B) Liver mass to BW ratio. (C) Hepatic triglyceride content. P-values of orthogonal *a priori* comparisons of the HFD versus each of the other groups are shown. $^{**}p < 0.01$, $^{***}p < 0.001$.

327 **5. RNA-seq reveals suppression of hepatic FA biosynthesis processes and pathways by**
328 **HXN and TXN treatments**

329 We conducted RNA-seq analysis of the livers obtained from mice after 16 weeks on the diet to
330 determine transcriptional mechanisms by which HXN and TXN supplementation could
331 ameliorate hepatic steatosis induced by HFD. Gene counts were calculated to quantify gene
332 expression in the four diet groups LFD, HFD, HFD+HXN, and HFD+TXN. The differentially
333 expressed genes (DEGs) were determined using a false discovery rate (FDR) cutoff of < 0.4, as
334 compared to HFD.

335 To visualize expression patterns of DEGs in the four groups we used hierarchical
336 clustering with a heat map (**Fig. 6A**). The DEGs clustered into two major types, one with higher
337 expression (red) in the LFD and HFD groups but lower expression (blue) in the HXN and TXN
338 groups and the other with lower expression in the LFD and HFD groups but higher expression in
339 the HXN and TXN groups (**Fig. 6A**). Individual mice clustered into two major nodes. All HFD
340 mice clustered with six LFD and four HXN mice and all TXN mice clustered with six HXN and
341 four LFD mice (**Fig. 6A**). This likely reflects the variability observed in phenotypic outcomes
342 (**Fig. 5 B-D**). The volcano plot analysis of gene expression revealed that both HXN and TXN
343 treatments induced significant changes in gene expression compared with the HFD group (**Fig.**
344 **6B**). TXN treatment had the greatest effect with 295 identified DEGs while HXN treatment only
345 resulted in six DEGs. We identified 212 DEGs in comparing the LFD and HFD groups.

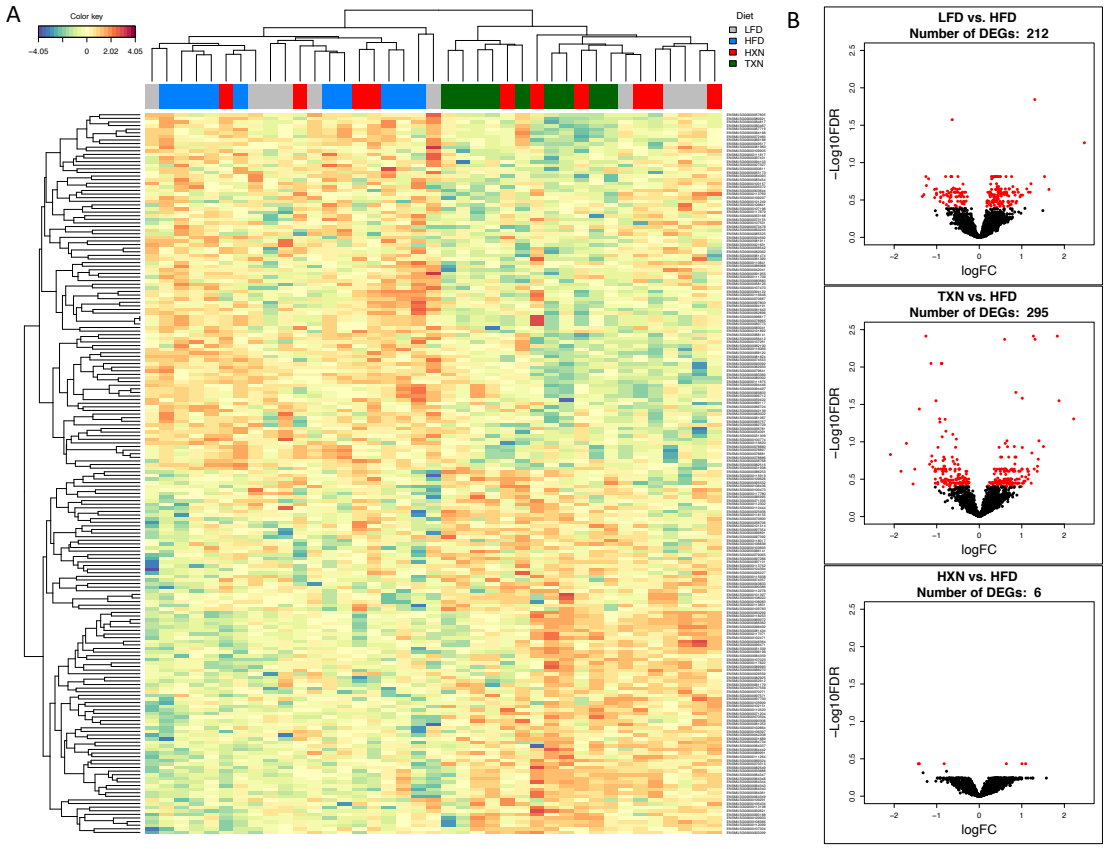

346

347 Figure 6. TXN treatment significantly alters liver transcriptome of mice after 16 weeks of feeding. (A)
348 Hierarchical clustering of the top 200 differentially expressed genes (DEGs) in each treatment group
349 (labeled at the top right corner: gray indicates LFD group, blue indicates HFD, red indicates HXN and
350 green indicates TXN.) as determined by RNAseq analysis. Color key is based on the $\log_2$ fold change. (B)
351 Volcano plots show DEGs (red dots) in the comparison of different treatment groups.

352 We next conducted gene ontology (GO) enrichment and pathway analysis of DEGs using
353 Enrichr (Chen *et al.*, 2013). We assigned the DEGs in the TXN treatment group to GO terms
354 describing biological processes. The enriched GO terms and pathways with adjusted p values <
355 0.05 are summarized in **Figure 7** and in the supporting information (individual Excel files). GO
356 enrichment analysis indicated that TXN treatment significantly downregulated genes involved in
357 biological processes including xenobiotic catabolism, FA metabolism, glucose metabolism and
358 regulation of lipid metabolism (**Fig. 7,** top panel). Furthermore, KEGG pathway analysis
359 demonstrated that TXN upregulated expression of genes in six pathways including complement
360 and coagulation cascades, prion diseases, steroid hormone biosynthesis, arachidonic acid
361 metabolism, retinol metabolism and linoleic acid metabolism (**Fig. 7,** bottom right panel). Many
362 of these included genes encoding Cyp450 enzymes. On the other hand, expression of genes in 25
363 KEGG pathways were significantly downregulated by TXN treatment compared to HFD (**Fig. 7,**
364 bottom left panel). The top 10 significantly enriched KEGG pathways based on statistical
365 significance and combined score ranking included the biosynthesis of unsaturated FAs,
366 glutathione metabolism, amino sugar and nucleotide sugar metabolism, glycolysis and
367 gluconeogenesis, pentose phosphate pathway, fluid shear stress and atherosclerosis, chemical
368 carcinogenesis, drug metabolism, FA elongation and the PPAR signaling pathway.

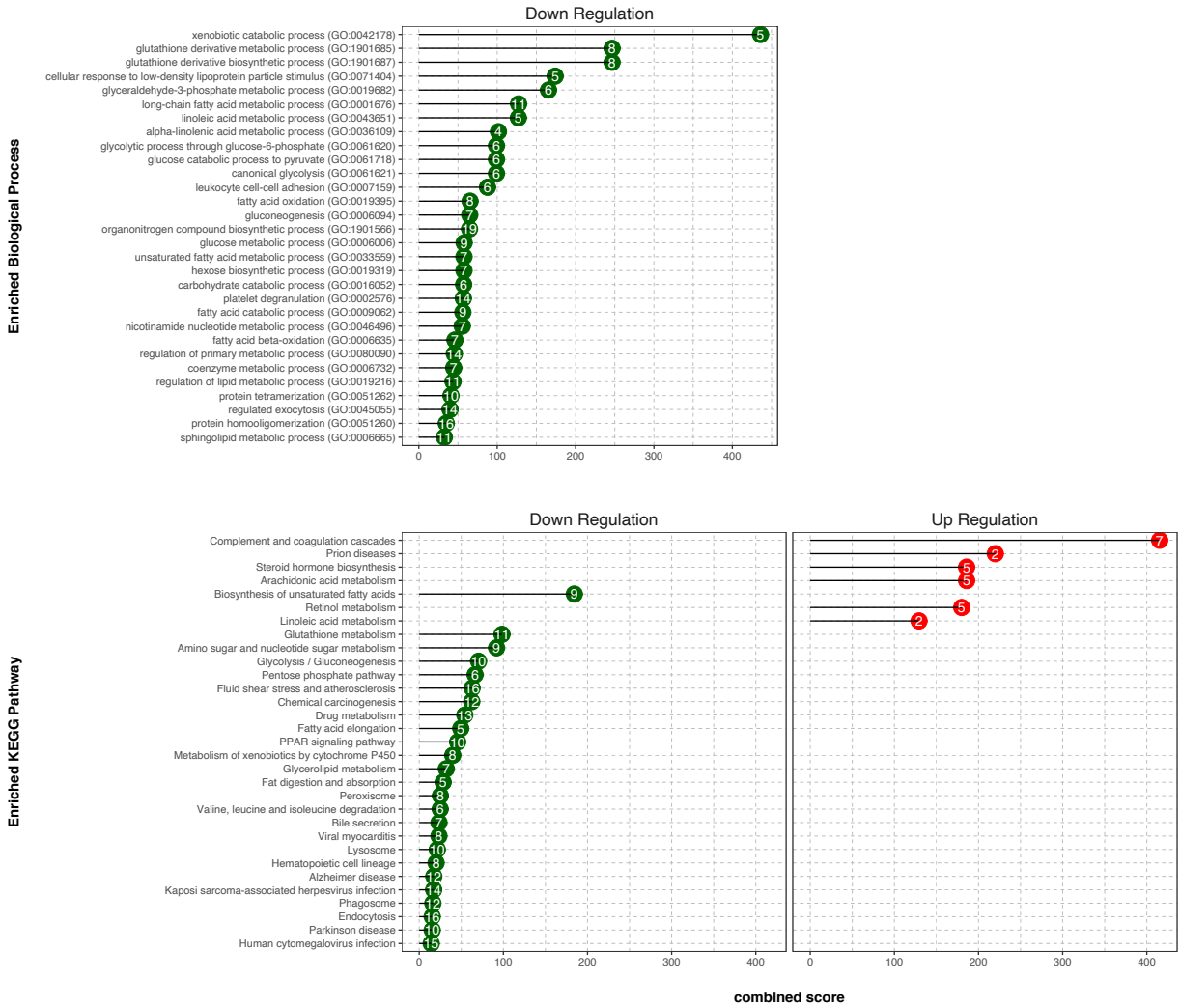

Figure 7. TXN decreases expression of numerous gene ontology and KEGG pathways. Analysis of DEGs from the livers of mice that consumed a HFD+TXN versus a HFD revealed mostly downregulation of biological processes and KEGG pathways. The significant (adjusted $p < 0.05$) enriched biological process terms in gene ontology (upper panel) and enriched KEGG pathways (lower panel) were selected by Enrichr Tools based on significance and combined scores. The number inside each lollipop represents the number of identified DEG genes in that specific biological process or KEGG pathway.

6. Identification of key hepatic genes regulated by TXN and involved in ameliorating hepatic steatosis

We implemented SVM to identify a set of signature genes that can distinguish TXN-treated mice from HFD-fed control mice. Briefly, we used the DaMirSeq R package to determine a set of genes whose principal components best correlated with TXN treatment by performing backward variable elimination with partial least-squares regression and removing redundant features by eliminating those that were very highly correlated (Chiesa, Colombo and Piacentini, 2018). Repeating this process 30 times, we used all 13 genes identified here as input into our SVM models (**Fig. 8,** left panel). Genes identified classified HFD- and TXN-fed mice into two distinct groups (**Fig. 8,** right panel). Eight of 13 genes showed significant, differential expression between TXN and HFD diet samples (**Table 1**). Consistent with the GO analysis, three of the eight genes – uncoupling protein 2 (*Ucp2*), cell death-inducing DFFA-like effector c (*Cidec*), and monoacylglycerol O-acyltransferase 1 (*Mogat1*) – are involved in lipid metabolism and known target genes of PPARγ (Medvedev *et al.*, 2001; Kim *et al.*, 2008; Matsusue *et al.*, 2008); (Bugge *et al.*, 2010; Karbowska and Kochan, 2012; Wolf Greenstein *et al.*, 2017).

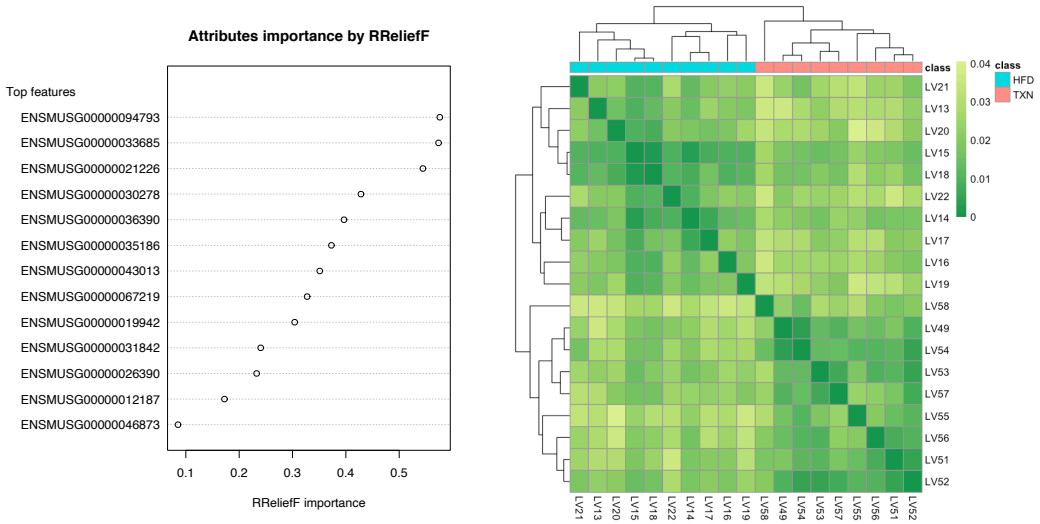

Figure 8. SVM identified signature genes that distinguish mice that consumed TXN. Left panel: the dot chart shows the top 13 genes, sorted by RReliefF importance score. This plot was used to select the most important predictors to be used for classification. Right panel: Colors in the heatmap highlight the distance matrix, obtained by Spearman's correlation metric: color gradient ranges from *dark green*, meaning "minimum distance" (i.e., dissimilarity = 0, correlation = 1), to *light green*. On the top of the heatmap, horizontal bars indicate HFD and HFD+TXN treatments. On the top and on the left side of the heatmap the dendrograms are shown. Plots were produced with DaMiRseq R package 1.10.0.

399 Table 1 Thirteen genes[a] used to distinguish TXN transcriptome from HFD transcriptome.

Ensemble ID	Gene name	Gene symbol	TXN vs. HFD (log_2 fold change)	P value	FDR
00000094793	major urinary protein 12	*Mup12*	2.65	***0.000***	0.011
00000033685	uncoupling protein 2	*Ucp2*	-1.07	***0.005***	0.109
00000036390	growth arrest and DNA-damage-inducible 45 alpha	*Gadd45α*	-0.32	0.420	0.800
00000021226	acyl-CoA thioesterase 2	*Acot2*	-1.33	***0.000***	0.003
00000030278	cell death-inducing DFFA-like effector c	*Cidec*	-2.41	***0.000***	0.006
00000043013	one cut domain, family member 1	*Onecut1*	1.53	***0.004***	0.098
00000067219	NIPA-like domain containing 1	*Nipal1*	0.22	0.630	0.890
00000035186	ubiquitin D	*Ubd*	-2.51	***0.002***	0.068
00000031842	phosphodiesterase 4C, cAMP specific	*Pde4c*	-0.30	0.370	0.770
00000026390	macrophage receptor with collagenous structure	*Marco*	0.73	0.120	0.560
00000012187	monoacylglycerol O-acyltransferase 1	*Mogat1*	-1.62	***0.000***	0.011
00000019942	cyclin-dependent kinase 1	*Cdk1*	-1.53	***0.009***	0.139
00000046873	membrane-bound transcription factor peptidase	*Mbtps2*	0.11	0.710	0.920

400 [a] Genes were ranked according to their *RReliefF* importance score using a multivariate filter technique
401 (*i.e., RReliefF*) (Chiesa et al., 2018). Also shown is the log_2 fold-changes, p values and FDR values when
402 HFD-TXN samples were compared with HFD samples using edgeR package (Robinson, McCarthy and
403 Smyth, 2010) in R. Negative values indicate genes down regulated in the liver with TXN
404 supplementation.

405 We then confirmed expression of these genes using RT-qPCR. Consistent with RNAseq
406 results, TXN-treated mice had significantly lower expression of major PPARγ target genes
407 *Cidec*, *Mogat1* and *Pparγ2,* a predicted PPAR target gene (Fang *et al.*, 2016) (**Fig. 9** top panel).
408 Moreover, we observed significantly strong positive correlations between the expression of these
409 three genes (**Fig. 9,** bottom panel). The above results suggest TXN treatment inhibits the PPARγ
410 pathway – a key pathway involved in hepatic lipid metabolism.

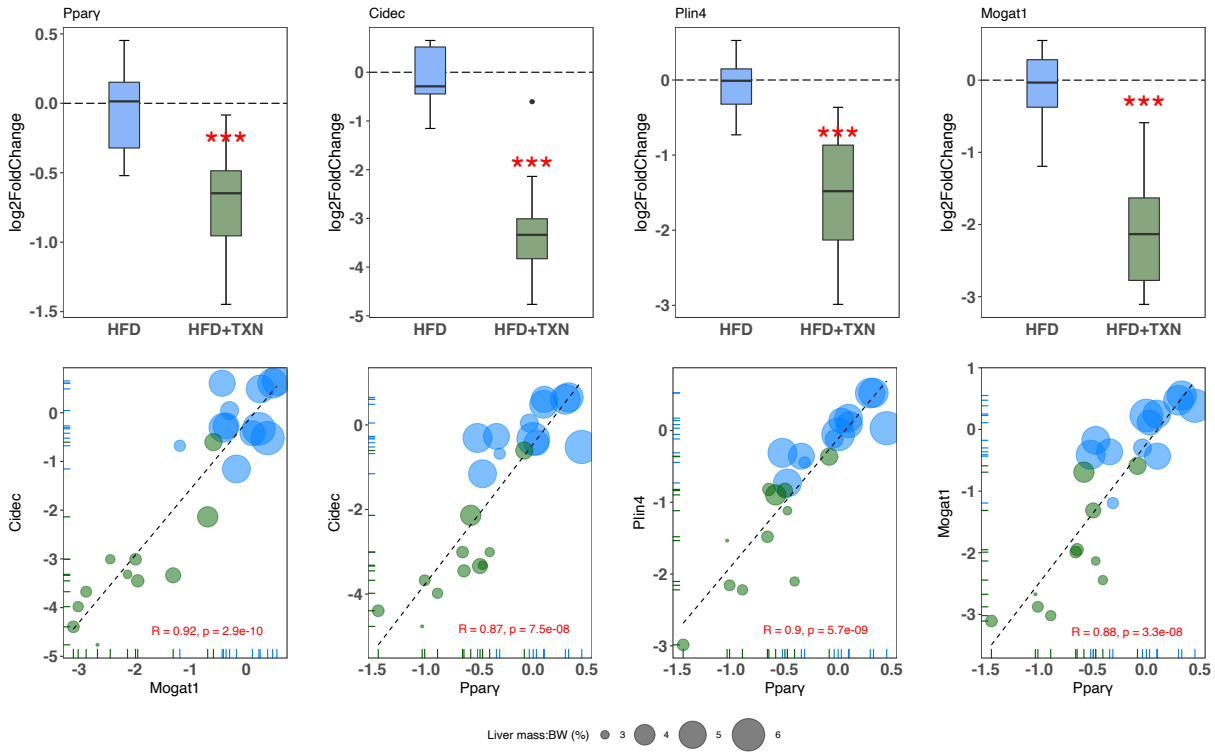

411

412 Figure 9. TXN-treated mice show significantly lower expression of PPARγ and target genes. Top panel:
413 reduction of HFD-induced *Pparγ2*, *Cidec*, and *Mogat1* expressions in the liver by TXN administration.
414 Mice were sacrificed after 16-week of HFD (blue, n = 12) or HFD+TXN (dark green, n = 11) feeding.
415 Liver tissues were harvested, and total RNA was extracted. Relative mRNA levels of selected genes were
416 determined by real time PCR. Gene expression is expressed in $\log_2$ fold change as quartiles. ***$p \leq$
417 0.001, t-test. Bottom panel: Pearson correlation between *Pparγ2* and *Cidec* or *Mogat1* expression. Data
418 are presented in $\log_2$ fold change; bubble size represents liver mass to BW ratio. • indicates sample
419 outside value, which is > 1.5 times the interquartile range beyond upper end of the box.

420 **7. XN and TXN do not produce cytotoxic effects in 3T3-L1 adipocytes**

421 Three groups have demonstrated that XN may affect adipocyte differentiation, but the
422 mechanism remains unclear (Yang *et al.*, 2007; Mendes *et al.*, 2008; Samuels,
423 Shashidharamurthy and Rayalam, 2018). We hypothesized that TXN and XN antagonizes the

424 PPARγ receptor, which would explain the decreased expression of its target genes. To test our
425 hypothesis, we utilized 3T3-L1 murine fibroblast cells, which depend on PPARγ activity to
426 differentiate into adipocytes (Tamori *et al.*, 2002).

427 XN and its derivatives are cytotoxic to some cells and to ensure that we used
428 concentrations that were not cytotoxic to 3T3-L1 adipocytes, we tested an escalating dose of XN
429 and TXN (Strathmann and Gerhauser, 2012). 3T3-L1 cells were treated with 0.1% DMSO, 1μM
430 rosiglitazone (RGZ), 1μM GW9662, XN 5-50 μM, TXN 5-50 μM, 25μM XN + 1μM RGZ or
431 25μM TXN + 1μM RGZ for 48 h. After treatments, we determined the number of live cells
432 using an MTT assay. XN and TXN were only significantly cytotoxic for 3T3-L1 cells at a dose
433 of 50 μM (data not shown). While it is difficult to translate *in vivo* doses to *in vitro* doses, based
434 on previous *in vitro* studies (Yang *et al.*, 2007; Samuels, Shashidharamurthy and Rayalam, 2018)
435 and our current cell viability data, we selected low (5 μM), medium (10 μM) and high (25 μM)
436 concentrations of XN and TXN for the subsequent experiments where cell viability was greater
437 than 90% (data not shown).

438 **8. XN and TXN attenuate intracellular lipid content in 3T3-L1 adipocytes in a dose**
439 **dependent manner**

440 XN inhibits murine preadipocyte 3T3-L1 differentiation and adipogenesis (Yang *et al.*, 2007;
441 Mendes *et al.*, 2008; Samuels, Shashidharamurthy and Rayalam, 2018); therefore, we determined
442 if TXN could inhibit 3T3-L1 adipocyte differentiation using the same model. The addition of
443 dexamethasone, IBMX and insulin strongly induced the intracellular lipid accumulation (**Fig. 10,**
444 **A2-3**). As expected, XN significantly attenuated intracellular lipid levels in a dose-dependent
445 manner (**B1-3**). Like XN, TXN also strongly inhibit intracellular lipid accumulation (**C1-3**).

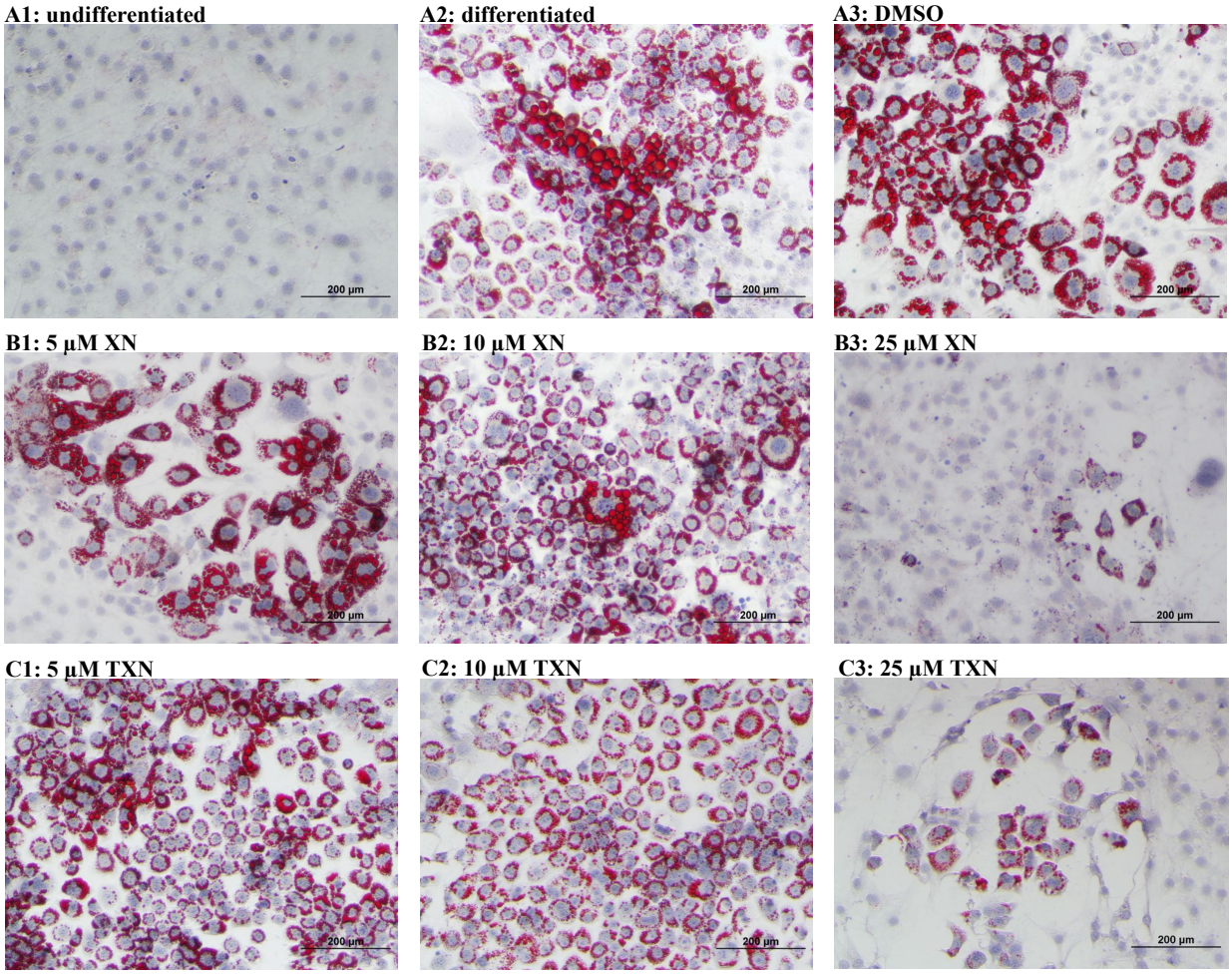

Figure 10. XN and TXN inhibit intracellular lipid accumulation in 3T3-L1 cells. 3T3-L1 cells ($1x10^6$ per well) in 12-well plates were cultured with either DMEM (A1), differentiation medium (DM) (A2), DM plus DMSO (A3), DM plus 5 µM XN (B1), DM plus 10 µM XN (B2), DM plus 25 µM XN (B3), DM plus 5 µM TXN (C1), DM plus 10 µM TXN (C2), or DM plus 25 µM TXN (C3). Cells were stained with oil red O to identify lipids at day 7 post-differentiation.

9. XN and TXN inhibit RGZ-induced adipocyte differentiation in 3T3-L1 cells in a dose dependent manner

RGZ is a known potent PPARγ agonist used as an insulin-sensitizing agent. To test the hypothesis that XN and TXN may antagonize PPARγ, we determined if the compounds would block RGZ-induced PPARγ actions (**Fig. 11**). RGZ strongly induced the differentiation (**Fig. 11**, **A1**), and GW 9662, a potent PPARγ antagonist, inhibited the RGZ-induced differentiation (**Fig. 11**, **A2**). We also observed that both XN (**Fig. 11**, **B1-3**) and TXN (**Fig. 11**, **C1-3**) suppressed RGZ-induced differentiation in a dose dependent manner. At 25 µM concentration, the RGZ-

460 induced differentiation was largely blocked (**Fig. 11**, **B3, C3**), suggesting that XN and TXN may
461 interfere or even compete with binding of RGZ to the PPARγ receptor.

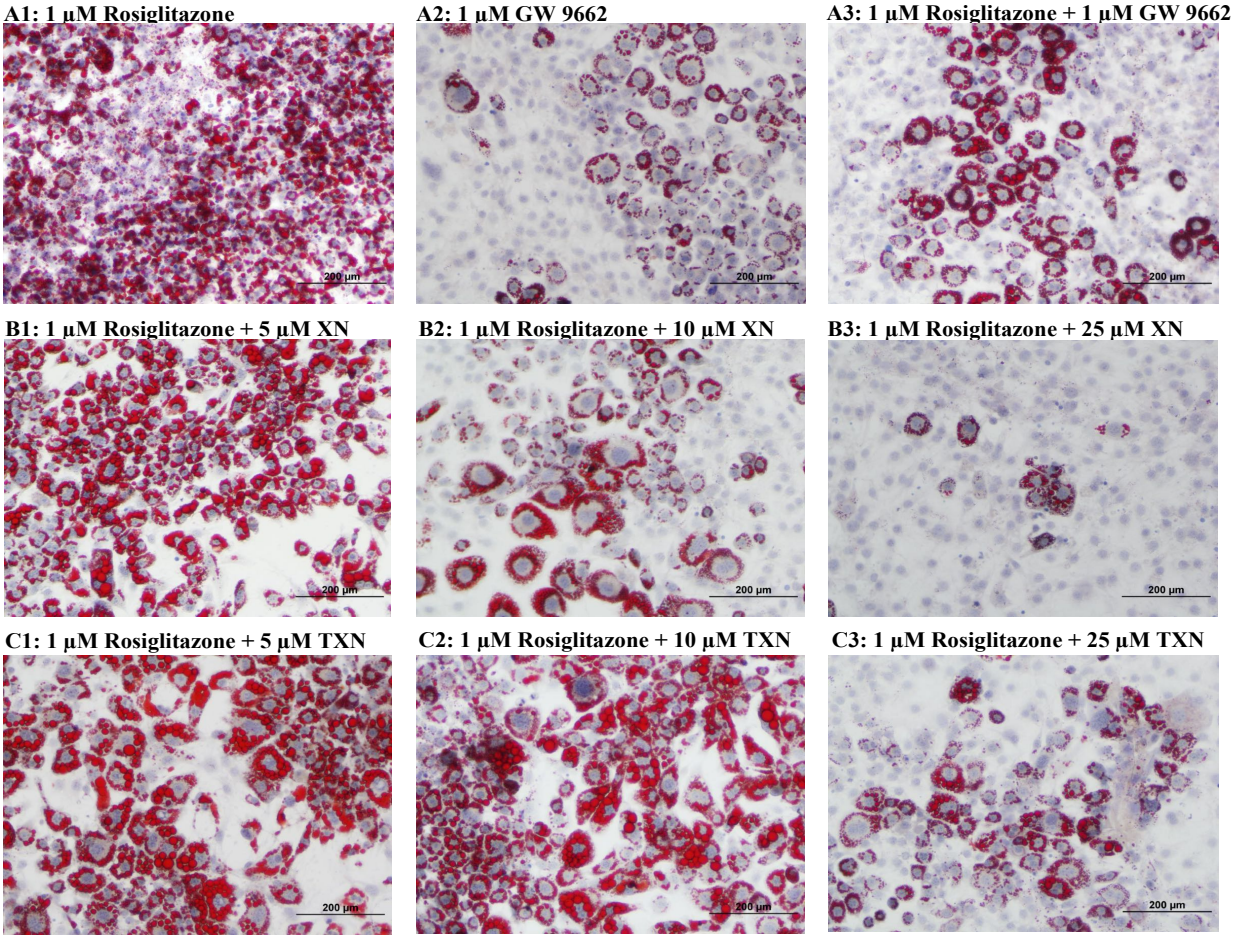

462

463 Figure 11. XN and TXN diminished the lipid accumulation in 3T3-L1 cells. 3T3-L1 cells ($1x10^6$ per well)
464 in 12-well plates were cultured with either DM plus 1µM rosiglitazone (A1), DM plus 1µM GW 9662
465 (A2), DM plus 1µM rosiglitazone and 1µM GW9662 (A3), DM plus 1 µM rosiglitazone and 5 µM XN
466 (B1), DM plus 1 µM rosiglitazone and 10 µM XN (B2), DM plus 1 µM rosiglitazone and 25 µM XN
467 (B3), DM plus 1 µM rosiglitazone and 5 µM TXN (C1), DM plus 1 µM rosiglitazone and 10 µM TXN
468 (C2), or DM plus 1 µM rosiglitazone and 25 µM TXN (C3). Cells were stained with oil red O to identify
469 lipids at day 7 post-differentiation.

470 **10. XN and TXN downregulate genes regulated by PPARγ in 3T3-L1 cells**

471 To elucidate the effect of XN and TXN on PPARγ action at the transcriptional level, we
472 measured the expression of several known PPARγ target genes using RT-qPCR on samples 7
473 days post 25 µM XN or TXN treatment. Consistent with the decrease of intracellular lipid
474 content in **Figures 10** and **11**, the expression of PPARγ and its target genes at 7 days post
475 treatment were significantly downregulated by XN and TXN treatments (**Table 2**). Cells treated

476 with 1 μM GW 9662, a PPARγ antagonist, did not significantly reverse the RGZ-induced
477 upregulation of these genes. Cells treated with either 25 μM XN or TXN significantly reversed
478 the RGZ-induced upregulation of *Cd36* ($p < 0.001$, $p < 0.001$), *Fabp4* ($p < 0.001$, $p < 0.001$),
479 *Mogat1* ($p < 0.001$, $p < 0.01$), *Cidec* ($p < 0.001$, $p < 0.001$), *Plin4* ($p < 0.001$, $p < 0.001$), *Fgf21*
480 ($p < 0.01$, $p < 0.01$). Taken together, these data above suggest that XN and TXN antagonize
481 PPARγ at the transcriptional level to block 3T3-L1 differentiation.

482 Table 2 Adipocyte gene expression at day 7 post-differentiation.

Gene	Log_2 (Fold Change)				p-values vs. RGZ		
	RGZ (cont)	RGZ + GW9662	RGZ + XN	RGZ + TXN	RGZ + GW9662	RGZ + XN	RGZ + TXN
Pparγ2	Ref.	-0.11	-1.93	-1.53	0.30	< 0.001	< 0.001
Cd36		-0.18	-9.10	-4.36	0.25	< 0.001	< 0.001
Fabp4		-0.12	-7.94	-4.08	0.43	< 0.001	< 0.001
Mogat1		-0.11	-4.16	-3.59	0.42	< 0.001	< 0.01
Cidec		-0.18	-10.10	-4.46	0.40	< 0.001	< 0.001
Plin4		-0.10	-3.01	-2.32	0.48	< 0.001	< 0.001
Fgf21		0.03	-0.99	-1.08	0.40	< 0.01	< 0.01

483 3T3-L1 differentiation was induced by IBMX, dexamethasone, insulin and 1 μM RGZ plus the addition
484 of 1 μM GW9662, 25 μM XN, or 25 μM TXN for 48 hours. After 48 hours, the old media was removed
485 and fresh DMEM was replenished for continuing differentiation. Gene expression was measured at day 7
486 post-differentiation using qRT-PCR. ΔCT = CT(target gene) – CT(reference gene). ΔΔCT = ΔCT(treated
487 sample) – ΔCT(untreated sample/control average). Fold change = $2^{-\Delta\Delta CT}$. Statistics were performed on
488 ΔΔCT values.

489 **11. XN and TXN antagonize ligand binding to PPARγ**

490 Based on the inhibition of RGZ induced adipocyte differentiation, and expression of PPARγ
491 target genes, we postulated that XN and TXN bind to the PPARγ ligand binding domain and
492 interfere with agonist binding. To test this hypothesis, we first performed a competitive binding
493 assay using a PPARγ TR-FRET assay. Both XN and TXN displaced a labelled pan-PPARγ
494 ligand in a dose-dependent manner with IC_{50} values of 1.97 μM (**Fig. 12B**) and 1.38 μM (**Fig.
495 12C**), respectively. Oleic acid, the most abundant FA ligand in the HFD diet (**Table 2**), had an
496 IC_{50} value of 16.6 μM. XN and TXN had similar IC_{50} values as the PPARγ ligand PGZ, a drug
497 used to improve insulin sensitivity and type 2 diabetes, and a natural ligand, arachidonic acid
498 (Chen *et al.*, 2012).

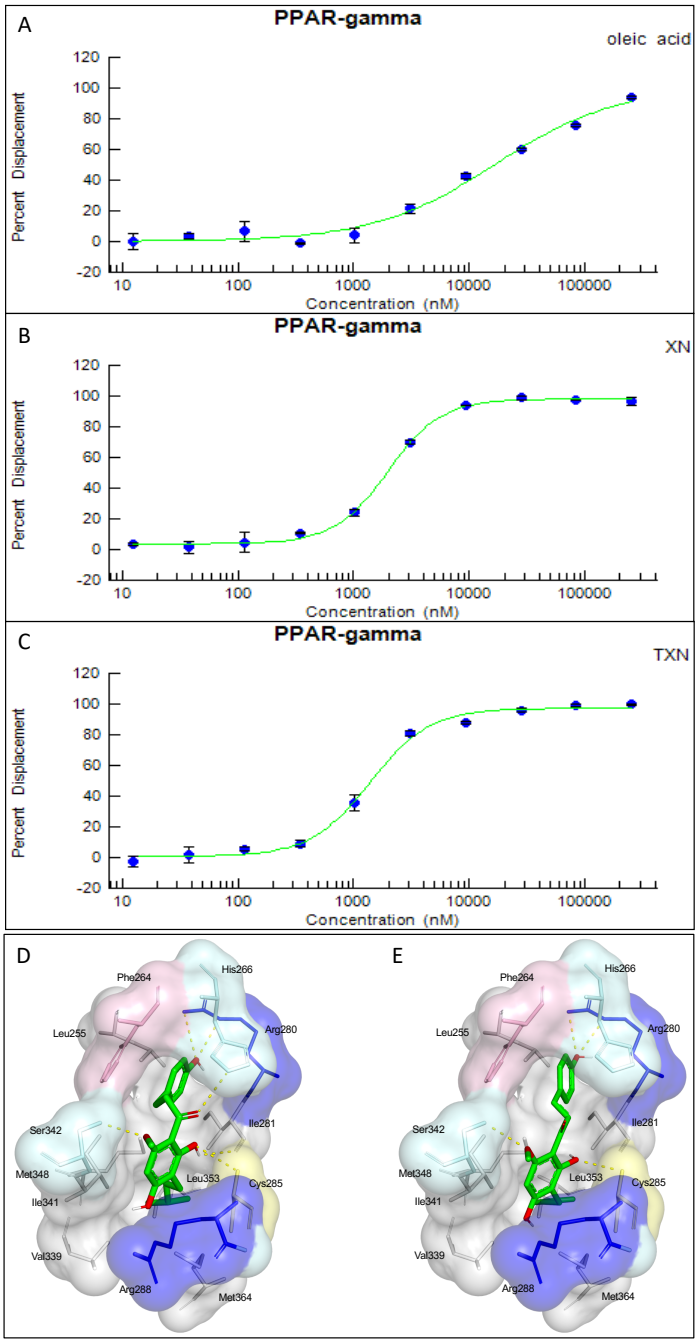

Figure 12. XN and TXN are ligands for PPARγ. A PPARγ nuclear receptor competitive binding assay based on time-resolved fluorescence resonance energy transfer (TR-FRET) was performed. The IC_{50} values for each compound was determined by % displacement of a pan-PPARγ ligand. (A) Oleic acid IC_{50} 16.6 µM. (B) XN IC_{50} 1.97 µM. (C) TXN IC_{50} 1.38 µM. Molecular docking studies show TXN and XN fit into the human PPARγ binding site. PPARγ residues containing atoms involved in hydrophobic interactions are shown. Yellow dashes indicate hydrogen bonds, amino acids colored as hydrophobic (grey), aromatic (pink), polar (cyan), basic (blue), or cysteine (yellow). (D) TXN (E) XN.

507 To obtain further insights into the interaction of XN and TXN with PPARγ, we analyzed
508 the nature of binding between the PPARγ-LBD and XN/TXN using molecular docking to
509 confirm the putative binding pose and position of XN/TXN and to estimate the relative binding
510 affinities of various ligands for PPARγ. To verify the robustness of our docking protocol,
511 resveratrol was re-docked into the bound structure of PPARγ, reproducing the binding pose and
512 orientation found in the crystal structure of the complex (PDB ID: 4JAZ). The best docked
513 position of TXN occupies the binding site of PPARγ, exhibiting many non-bonded interactions
514 involving side chain atoms in Leu255, Phe264, Gly284, Cys 285, Arg288, Val339, Ile 341,
515 Met348, and Met364 (**Fig. 12 D**). The side chains of His266, Arg280, and Ser342 and the main
516 chain carbonyl oxygen atom of Ile281 are well positioned to make electrostatic/hydrogen bonds
517 with the hydroxyl protons and oxygen atoms of the bound TXN molecule. We observed many of
518 the same hydrophobic interactions in the simulated PPARγ-XN (**Fig. 12 E**) and PPARγ-oleic
519 acid complexes, and potential electrostatic interactions between His266 and Glu343, or with
520 Arg280 and XN or oleic acid, respectively. The relative binding affinities, ranked in decreasing
521 value of their negative binding energies were, in order, TXN, XN, and oleic acid, consistent with
522 the TR-FRET binding results.

523 ## Discussion

524 **XN and TXN are effective in suppressing development of diet-induced steatosis**

525 Low cost natural products like XN are of particular interest for treating obesity and NAFLD due
526 to their availability, safety and efficacy. XN and its derivatives appear to function through
527 multiple mechanisms of action that may enhance their effectiveness. Three studies propose that
528 XN improves diet-induced hepatic steatosis by suppressing SREBP1c mRNA expression and
529 SREBP activation (Yui, Kiyofuji and Osada, 2014; Miyata *et al.*, 2015; Takahashi and Osada,
530 2017). We also observed a decrease in hepatic SREPB1c expression with TXN treatment. Others
531 propose mechanisms include inhibiting pro-inflammatory gene expression (Dorn *et al.*, 2010;
532 Mahli *et al.*, 2019), inducing AMPK activation in the liver and skeletal muscle (Costa *et al.*,
533 2017), and enhanced FA oxidation (Kirkwood *et al.*, 2013). In this study, using a combination of
534 molecular, biochemical, biophysical and bioinformatics approaches, we provide evidence for an
535 additional novel mechanism by which XN and its derivative, TXN, can inhibit diet-induced

536 hepatic steatosis through downregulation of hepatic FA uptake and lipid storage by binding to
537 PPARγ in the liver and effectively antagonizing its actions.
538 We previously demonstrated that XN and TXN ameliorated DIO in C57Bl6/J mice with
539 no evidence of liver injury (Miranda *et al.*, 2018). Using the same animal model, we confirmed
540 the phenotypic outcomes observed in the previous study (**Fig. S1**). In this study and prior studies
541 (Miranda *et al.*, 2018), we noted a decrease in weight with treatment in the presence of similar
542 caloric intake. Our metabolic cage data demonstrated energy expenditure increased with body
543 mass, but a treatment effect was not identified. We hypothesize that changes in microbiota
544 composition and bile acid metabolism which can affect nutrient and energy harvesting may
545 explain the reduction in weight (Wahlström *et al.*, 2016; Zhang *et al.*, 2020) observed by
546 treatment, but requires testing in future work. Furthermore, we demonstrated the effect of XN
547 and TXN on the development and progression of diet-induced hepatic steatosis. Administration
548 of XN (60 mg/kg BW) and TXN (30 mg/kg BW) significantly slowed the development and
549 progression of hepatic steatosis during a 16-week high fat feeding. We observed less macro- and
550 microvesicular steatosis, significantly lower liver mass to BW ratio, decreased TAG
551 accumulation, and significantly lower steatosis scores in the XN and TXN supplemented mice
552 compared to their untreated HFD mice (**Figs. 2B & 4**). Four pathways generally maintain hepatic
553 lipid homeostasis: uptake of circulating lipids, *de novo* lipogenesis (DNL), FA oxidation (FAO)
554 and lipid export in very low-density lipoproteins (VLDL). These pathways are under tight
555 regulation by hormones, nuclear receptors, and other transcription factors (Bechmann *et al.*,
556 2012). Long-term dysregulation of one and/or multiple processes can lead to the development of
557 NAFLD, obesity, type 2 diabetes and other metabolic disorders.
558 To elucidate the mechanism of XN and TXN, we determined liver transcriptomic
559 changes after 16 weeks of HFD feeding using RNAseq. We observed significant changes in
560 hepatic gene expression with TXN administration (**Fig. 6 B**). GO enrichment analysis of DEGs
561 revealed that several biological processes were significantly downregulated by TXN treatment,
562 including xenobiotic catabolism, FA metabolism, glucose metabolism and regulation of lipid
563 metabolism (**Fig. 7**). Furthermore, KEGG pathway analysis of DEGs revealed multiple
564 biological pathways were downregulated in the livers of TXN-treated mice, including
565 biosynthesis of unsaturated FAs, glutathione metabolism, amino sugar and nucleotide sugar
566 metabolism, glycolysis and gluconeogenesis, FA elongation, and PPAR signaling pathways,

567 suggesting that TXN rewired global hepatic lipid metabolism (**Fig. 7**). There was a paucity of
568 differentially expressed genes in the livers of mice supplemented with a high dose of XN (60
569 mg/kg BW) even at an FDR cutoff of 0.4. This discrepancy might be due to reduced levels of
570 XN in peripheral tissues as compared with TXN as we previously observed a 12-fold lower level
571 of XN as compared with TXN in the liver (Miranda *et al.*, 2018).
572 To discover signature genes in the liver of mice treated with TXN, we applied a SVM
573 classifier algorithm and extracted the most important features (genes) (**Fig. 8**). Due to the limited
574 number of samples in this study, we did not separate the data into training and testing sets for the
575 construction of SVM. The caveat of this is that the learning model might not generalize well.
576 Consistent with GO analysis, three out of the eight significantly regulated genes – uncoupling
577 protein 2 (*Ucp2*), cell death-inducing DFFA-like effector c (*Cidec*), and monoacylglycerol O-
578 acyltransferase 1 (*Mogat1*) – are involved in lipid metabolism **(Table 1)**. Notably, these genes
579 are targets of PPARγ (Bugge *et al.*, 2010; Karbowska and Kochan, 2012; Wolf Greenstein *et al.*,
580 2017). PCR confirmed this finding (**Fig. 9**) and suggests that TXN modulates PPARγ actions.

581 **XN and TXN are novel natural and synthetic PPARγ antagonists**

582 PPARγ belongs to a superfamily of nuclear receptors and just like other members, its
583 activity requires ligand binding. PPARγ is highly expressed in white and brown adipose tissue,
584 and to a lesser extent in the liver, kidney, and heart (Zhu *et al.*, 1993; Lee and Ge, 2014).
585 Because of its essential role in regulating adipogenesis and higher expression in the white
586 adipose tissue, PPARγ has been a pharmacological target for drug development (Lehmann *et al.*,
587 1995; Lefterova *et al.*, 2014) in combating metabolic diseases such as insulin resistance and type
588 2 diabetes. Thiazolidinediones (TZDs), which include RGZ and PGZ, are the most widely
589 investigated PPARγ agonists due to their strong insulin-sensitizing ability (Henney, 2000;
590 Soccio, Chen and Lazar, 2014). Studies show that the main action of TZDs occurs in adipocytes
591 (Chao *et al.*, 2000). In the liver, PPARγ plays a role in hepatic lipogenesis (Sharma and Staels,
592 2007). Multiple clinical trials using TZDs have observed significant improvement in hepatic
593 steatosis and inflammation (Ratziu *et al.*, 2008, 2010; Sanyal *et al.*, 2010), suggesting additional
594 actions of TZDs in non-adipocytes. Interestingly, PGZ is more effective in treating fatty liver
595 disease than RGZ, the more potent PPARγ agonist (Promrat *et al.*, 2004; Ratziu *et al.*, 2008,
596 2010), suggesting a moderate binding is more effective. Unfortunate side effects of TZDs are
597 weight gain (Fonseca, 2003), bone loss (Schwartz and Sellmeyer, 2007; Schwartz, 2008), edema

598 and increased risk of cardiovascular complications (Nesto *et al.*, 2004; Yang and Soodvilai,
599 2008; Bełtowski, Rachańczyk and Włodarczyk, 2013), due to over-activation of PPARγ. Thus,
600 there is great interest in identifying "ideal" PPARγ modulators that are tissue specific with
601 limited side effects.

602 An alternative strategy that aims to repress PPARγ has emerged in recent years
603 (Ammazzalorso and Amoroso, 2019). The potential of reducing BW and improving insulin
604 sensitivity suggests a possible clinical role of PPARγ antagonists in treating obesity and type 2
605 diabetes (Yamauchi *et al.*, 2001; Rieusset *et al.*, 2002; Nakano *et al.*, 2006). Compared to
606 agonists, researchers have identified only a few natural compounds that inhibit PPARγ, all of
607 which have a moderate binding affinity for PPARγ receptor and can inhibit adipogenesis, obesity
608 and/or hepatic steatosis. These include resveratrol (Calleri *et al*., 2014), 7-chloroarctinone-b
609 isolated from the roots of *Rhaponticum uniflorum* (Li *et al.*, 2009), tanshinone IIA from the roots
610 of *Salvia miltiorrhiza* (danshen) (Gong *et al.*, 2009), astaxanthin from red-colored aquatic
611 organisms (Jia *et al.*, 2012), protopanaxatriol (PPT) extracted from *Panax ginseng* roots (Zhang
612 *et al.*, 2014), foenumoside B from the herbal plant *Lysimachia foenum-graecum* (Kwak *et al.*,
613 2016), and betulinic acid, a pentacyclic triterpene found in the bark of several plants (Brusotti *et*
614 *al.*, 2017; Ammazzalorso and Amoroso, 2019).

615 Several lines of evidence presented in this study supports the hypothesis that XN and
616 TXN are also PPARγ antagonists. First, using the 3T3-L1 cell model for PPARγ-mediated
617 adipogenesis, we demonstrated that XN and TXN significantly and strongly suppressed RGZ
618 induced adipocyte differentiation and adipogenesis by day 7 (**Fig. 11**). Consistent with a
619 decrease in lipid accumulation, PPARγ target genes were also significantly downregulated in XN
620 and TXN-treated cells (**Table 2**). The PPARγ antagonist, GW9662, did not significantly affect
621 target gene expression of PPARγ, even though it clearly inhibited differentiation (**Fig.10 A2-3**).
622 In our experiments, we used a significantly lower concentration of GW9662 than used by others
623 that ranged from 3-25 times higher, and this difference could explain our results (Park *et al.*,
624 2008; Kim, Nian and McIntosh, 2011; Sankella, Garg and Agarwal, 2016). Second, the PPARγ
625 nuclear receptor competitive binding assay showed that XN and TXN have a moderate binding
626 affinity of 1.97 μM and 1.38 μM, respectively (**Fig. 12**). Lastly, consistent with the competitive
627 binding assay, simulated molecular docking indicated that XN and TXN can interact with the
628 ligand binding domain of PPARγ like other known ligands and potentially form hydrogen bonds

629 with His266, Arg280, Ser342 and Ile281, in addition to many non-bonded interactions (**Fig. 12**
630 **DE**). Moreover, the predicted binding model reveals that the interactions between XN, TXN and
631 the PPARγ ligand binding domain resembles those observed between PPARγ and resveratrol, a
632 dietary polyphenol that is also a PPARγ antagonist (Calleri *et al.*, 2014). Our findings are
633 consistent with XN and TXN functioning as PPARγ antagonists.
634 One of the many side effects observed from TZD therapy is weight gain. TZDs primarily
635 mediate their effects in adipose tissue by PPARγ activation that stimulates adipocyte
636 differentiation and increases the efficiency of uptake of circulating non-esterified FAs (NEFA)
637 by adipocytes (Rosen and Spiegelman, 2006). Interestingly, in this study, we observed a
638 significant decrease in overall, mWAT, and sWAT fat mass in HXN- and TXN-treated mice
639 (**Figs. 2A, 4AC**), yet a slight increase in the eWAT fat mass (**Fig. 4B**). Prior studies have
640 reported that the expandability of eWAT in male mice is an indicator of metabolic health. Mouse
641 sWAT and mWAT will continue to expand with BW, whereas eWAT expansion diminishes after
642 mouse BW reaches about 40 g (van Beek *et al.*, 2015). Our data suggest that HXN- and TXN-
643 treated mice have capacity to expand eWAT, whereas HFD-fed untreated mice do not, which
644 seems to direct the development of metabolic disorders. In our previous study, we demonstrated
645 that XN and TXN accumulates primarily in the liver with significantly lower levels in the muscle
646 (Miranda *et al.*, 2018). We could not detect XN or TXN in the WAT of these mice (data not
647 shown). The levels of XN and TXN in the liver (TXN > HXN > LXN) and the absence of both
648 compounds in the WAT suggests that these compounds antagonize PPARγ in the liver and not in
649 the WAT, therefore, minimizing the side effect of weight gain observed with TZDs that are
650 PPARγ agonists.
651 During a long term HFD feeding, PPARγ and its target genes are upregulated to
652 compensate for the lipid overflow in the liver (**Fig. 13**, top panel). Namely, genes associated with
653 lipid uptake and trafficking (*Lpl*, *Cd36*, *Fabp4*), TAG synthesis (*Fasn*, *Scd1*, *Mogat1*), and
654 formation of lipid droplets for storage (*Cidec*/*Fsp27*, *Plin4*) (Supplement_File_B). The result is
655 excessive lipid accumulation in the liver, leading to hepatic steatosis. This was observed with
656 PPARγ overexpression in hepatocytes in *ob/ob* mice (Wolf Greenstein *et al.*, 2017). We propose
657 that TXN added to a HFD antagonizes PPARγ action in the liver potentially by physically
658 interacting with PPARγ receptors as indicated in the molecular docking studies (**Fig. 12 DE**)
659 and; therefore, reduces PPARγ transcriptional activity and expression of the aforementioned

660 target genes. Several *in vivo* studies support our findings. Liver-specific PPARγ deficiency
661 protects *ob/ob* mice from hepatic steatosis (Matsusue *et al.*, 2003); knockdown of *Mogat1* in the
662 liver significantly attenuates hepatic steatosis after 12 weeks HFD feeding (Lee *et al.*, 2012); and
663 restoration of CIDEC/FSP27 in *ob/ob* liver-specific PPARγ knockout mice promotes hepatic
664 steatosis (Matsusue *et al.*, 2008). The role for PLIN4 in hepatic steatosis is limited, but it may
665 affect TAG accumulation during HFD feeding (Griffin *et al.*, 2017).
666 In conclusion, we demonstrated that TXN is very effective in suppressing the
667 development and progression of diet induced hepatic steatosis in mice. TXN appears more
668 effective in-vivo than XN perhaps due to TXN level is significantly higher in the liver, but XN
669 can slow progression of the condition at a higher dose. We provide evidence that XN and TXN
670 act as novel, natural and synthetic antagonists of PPARγ that bind with a similar affinity as the
671 agonist PGZ. Our findings support further development of XN and TXN as novel, low-cost
672 therapeutic compounds for diet-linked hepatic steatosis with fewer negative side effects than
673 current drugs, such as less adipose tissue expansion. Additionally, the structures of XN and TXN
674 could serve as scaffolds for the synthesis of more effective compounds for the treatment of fatty
675 liver diseases such as NAFLD. Although these results are encouraging, further studies are
676 required to clarify possible use in humans for the prevention and treatment of diet-linked hepatic
677 steatosis.

678 ## Materials and Methods

679 **Animals and diets**

680 Studies were performed in 8-week-old SPF male C57BL/6J mice obtained from The Jackson
681 Laboratory (Bar Harbor, ME, USA). Upon arrival, mice were housed individually in ventilated
682 cages in a controlled environment (23 ± 1ºC, 50-60% relative humidity, 12 hours daylight cycle,
683 lights off at 18:25 hours) with food and water *ad libitum*. After acclimating mice for one week on
684 a normal-chow diet (PicoLab Rodent Diet 20, 5053, TX, USA) followed by two-weeks on a low-
685 fat control diet (LFD, Dyets Inc., Bethlehem, PA, USA), they were randomly assigned to five
686 groups (n = 12/group). The groups were fed either a LFD, HFD, HFD + 30 mg/kg BW/day XN
687 (LXN), HFD + 60 mg/kg BW/day XN (HXN), or HFD + 30 mg/kg BW/day TXN (TXN). The
688 sources and purity of XN and TXN were described previously (Miranda *et al.*, 2018). The

689 chemical structures of XN and TXN, a detailed diet composition and FA composition are
690 available in **Figure 1**, **Table 3** and **Table 4**, respectively.

691 Table 3 Composition of diets[a]

	HFD	HFD+LXN	HFD+HXN	HFD + TXN	LFD
Ingredient (g/100g)					
Casein	2.58	2.58	2.58	2.58	1.89
L-Cystine	0.04	0.04	0.04	0.04	0.03
Sucrose	0.89	0.89	0.89	0.89	0.89
Cornstarch	0.00	0.00	0.00	0.00	4.02
Cellulose	0.54	0.54	0.54	0.54	0.47
Dyetrose	1.62	1.62	1.62	1.62	1.62
Soybean Oil	0.32	0.32	0.32	0.32	0.24
Lard	3.17	3.17	3.17	3.17	0.19
Mineral Mix #210088	0.13	0.13	0.13	0.13	0.10
Dicalcium Phosphate	0.17	0.17	0.17	0.17	0.12
Calcium Carbonate	0.07	0.07	0.07	0.07	0.05
Potassium Citrate H_2O	0.21	0.21	0.21	0.21	0.16
Vitamin Mix #300050	0.13	0.13	0.13	0.13	0.10
Choline Bitartrate	0.03	0.03	0.03	0.03	0.02
Test compound	0.00	0.003	0.006	0.003	0.00
OPT	0.10	0.10	0.10	0.10	0.10
Composition (kcal%)					
Protein	20	20	20	20	20
Carbohydrates	20	20	20	20	70
Lipids	60	60	60	60	10
Energy Density (kcal/g)	5.12	5.12	5.12	5.12	3.55

692 [a]LXN provides 30 mg/kg BW xanthohumol (XN), HXN 60 mg/kg XN, and TXN 30 mg/kg Tetrahydro-
693 XN (TXN) per day. The test compounds were dissolved in an isotropic mixture of oleic acid: propylene
694 glycol: Tween 80 (OPT) 0.9:1:1 by weight before incorporation into the diets. All diets were purchased
695 from Dyets Inc., Bethlehem, PA, USA.

696 Table 4 Fatty acid composition (% of the total fat) of the low-fat diet (LFD) and high-fat diet (HFD).

Fatty Acids	**% of the total fat**		**g/kg diet**	
	LFD	HFD	LFD	HFD
14:0 Myristic	0.7	1.4	0.29	4.75
16:0 Palmitic	17.0	24.2	7.28	84.34
16:1 Palmitoleic	1.5	3.1	0.65	10.76
18:0 Stearic	8.3	12.3	3.56	42.92
18:1 Oleic	32.2	42.1	13.76	146.95
18:2 Linoleic	35.2	14.9	15.04	51.89
18:3 Linolenic	5.0	2.1	2.14	7.27
SFAs	26.0	37.9	11.13	132.01
MUFAs	33.7	45.2	14.41	157.71
PUFAs	40.2	17.0	17.18	59.16
Total n-6 PUFA	35.2	14.9	15.04	51.89
Total n-3 PUFA	5.0	2.1	2.14	7.27

697 Abbreviations: SFA: saturated fatty acids; MUFAs: monounsaturated fatty acids; PUFAs:
698 polyunsaturated fatty acids; n-6: omega-6 fatty acids; n-3: omega-3 fatty acids.

699 BW gain and food intake of individual mice were assessed once per week. Body
700 composition was determined at the end of the feeding using a Lunar PIXImus 2 Dual Energy X-
701 ray Absorptiometer (DXA) scan (Madison, WI, USA). After 16 weeks of feeding the control and
702 test diets, mice were fasted for 6 h during the dark cycle, anaesthetized in chambers saturated
703 with isoflurane and then euthanized by cardiac puncture followed with cervical dislocation.
704 Blood was collected in syringes containing 2 IU of heparin and centrifuged to separate plasma
705 from cells. The liver and sWAT, mWAT, and eWAT fat pads were carefully collected and
706 weighed. The Institutional Animal Care and Use Committee (IACUC) at Oregon State
707 University approved all animal work (ACUP 5053). Animal experiments were performed in
708 accordance with the relevant guidelines and regulations.

709 **Liver histology**

710 Liver (~100 mg) was freshly collected from mice and immediately fixed overnight in 10%
711 neutrally buffered formalin, paraffin embedded, sectioned, and stained with hematoxylin-eosin
712 (Veterinary Diagnostic Laboratory, Oregon State University, OR). Each slide contained two liver
713 sections that were examined using a Leica microscope at 100× magnification. Representative
714 images were taken at 100× magnification from the subjectively least and most severely affected
715 areas ensuring representation of all zones of the hepatic lobule. Steatosis was objectively

716 quantified as percent surface area occupied by lipid vacuoles using ImageJ for image analysis
717 (NIH; imagej.nih.gov/ij/index.html) as previously published (Garcia-Jaramillo *et al.*, 2019).

718 **Energy expenditure**

719 Indirect calorimetry measurements were based on an open respirometer system. From week 10,
720 mice were housed individually in Promethion® Line metabolic phenotyping chambers (Sable
721 Systems International, Las Vegas, NV, USA) and maintained on a standard 12 h light/dark cycle
722 for three days. The system consisted of 10 metabolic cages, each equipped with food and water
723 hoppers connected to inverted laboratory balances for food intake monitoring; both food and
724 water were available *ad-libitum*. Spontaneous physical activity (SPA) was quantified via infrared
725 beam breaks in X and Y axes, and included locomotion, rearing, and grooming behaviors (BXY-
726 R, Sable Systems International). All raw data from all sensors and analyzers were stored every
727 second. Air within the cages was sampled through micro-perforated stainless-steel sampling
728 tubes located around the bottom of the cages, above the bedding. Ambient air was passed
729 through the cages (2 L/min) and gases were sampled continuously for each cage, allowing the
730 simultaneous acquisition of metabolic data every second, for all cages in the system (Lighton and
731 Halsey, 2011). The energy expenditure was estimated from oxygen consumption (VO_2) and
732 carbon dioxide production (VCO_2) rates by the Promethion system using the Weir formula.

733 **Liver tissue RNA extraction and library preparation**

734 Freshly dissected liver tissue was flash frozen in liquid N_2 and then stored at -80ºC. Total RNA
735 was isolated using the Direct-zol RNA Miniprep Plus kit as instructed (Zymo Research, Irvine,
736 CA, USA). RNA concentrations were quantified using the Qubit™ 1.0 Fluorometer and the
737 Qubit RNA BR Assay kit (Thermo Fisher Scientific, Waltham, MA, USA). RNA purity and
738 integrity were evaluated using a Bioanalyzer RNA 6000 Nano chip (Agilent Technologies, Santa
739 Clara, CA, USA). Samples ranged from medium to high RNA quality (RIN 5.9-8.3), and
740 samples with different RIN values showed similar RNA-seq qualities.

741 Each library was prepared with 325 ng total RNA using the Lexogen QuantSeq 3'mRNA-
742 Seq Library Prep Kit-FWD for Illumina sequencing according to the manufacturer's instructions
743 (Lexogen GmbH, Vienna, Austria). Briefly, library preparation was started by oligo(dT) priming,
744 with primers already containing the Illumina-compatible linker sequence for Read 2. After first-
745 strand synthesis, the RNA was removed before random primers that contained the corresponding
746 Illumina-compatible linker sequence for Read 1 initiated the second-strand synthesis. Second

747 strand synthesis was followed by a magnetic bead-based purification step. The libraries were
748 PCR amplified introducing sequences required for cluster generation and i7 and i5 dual indices
749 (Lexogen i7 6 nt Index Set and Lexogen i5 6 nt Unique Dual Indexing Add-on Kit) for 16-20
750 PCR cycles with the optimal number predetermined by qPCR with the PCR Add-on Kit for
751 Illumina (Lexogen GmbH). After a second magnetic bead-based purification, libraries were
752 quantified using the Qubit dsDNA HS Assay Kit (Thermo Fisher Scientific) and sized using an
753 Agilent High Sensitive D5000 Screen Tape (Agilent Technologies) to determine molarity. Equal
754 molar amounts of the libraries were multiplexed and then sequenced on an Illumina Hiseq3000
755 platform (Illumina, San Diego, CA, USA) at the Center for Genome Research and
756 Biocomputing, Oregon State University using single-end sequencing with 100-bp reads.
757 Approximately 6.6 million reads were obtained per liver sample.

758 **Sequence alignment and gene counts**

759 Adaptors and low quality tails were trimmed and ribosomal rRNA contaminations were removed
760 using BBDuk from the BBTools toolset (Bushnell, 2014). As recommended by the manufacturer
761 (Lexogen GmbH), a Phred score of 10 and a read length of 20 were used as the minimum cutoff
762 prior to data analysis (https://www.lexogen.com/quantseq-data-analysis/). Using a splice-aware
763 aligner STAR (Dobin *et al.*, 2013) (version 37.95), cleaned reads were then mapped against the
764 GRCm38 primary assembly of the *Mus musculus* genome (version mm10, M22 release)
765 (ftp://ftp.ebi.ac.uk/pub/databases/gencode/Gencode_mouse/release_M22/GRCm38.primary_asse
766 nbly.genome.fa.gz) with the annotation file of the same version
767 (ftp://ftp.ebi.ac.uk/pub/databases/gencode/Gencode_mouse/release_M22/gencode.vM22.annotati
768 on .gtf.gz), both from the GENCODE project (Frankish *et al.*, 2019). On average, over 81% of
769 the reads were uniquely mapped for each sample. Downstream analyses were based on uniquely
770 aligned reads.

771 To generate count matrices from bam files, the summarizeOverlaps function from the
772 GenomicAlignments package (v1.8.4) was used (Lawrence *et al.*, 2013). The location of the
773 exons for each gene was obtained from a transcript database (TxDb) using the
774 makeTxDbFromGFF function from the GenomicFeatures package (version 1.24.4), with a pre-
775 scanned GTF file used in the mapping step. Genes were then annotated with the R package Mus
776 musculus (version 1.3.1) (Team, 2016).

777 **Identification of differentially expressed genes (DEGs)**

778 R package edgeR (version 3.26.8) was used to detect differential change in gene expression
779 among mice on different diets (Robinson, McCarthy and Smyth, 2010). Genes expressed in at
780 least nine samples were retained using the filterByExpr function in edgeR. Unannotated genes,
781 pseudogenes and ribosomal RNA genes were also removed from downstream analyses. Gene
782 counts were then normalized with the default TMM (trimmed mean of M-values) method
783 (Robinson and Oshlack, 2010) provided by edgeR. To account for both biological and technical
784 variability, an overdispersed Poisson model and an Empirical Bayes method were used to
785 moderate the degree of overdispersion across transcripts. Genes with a false discovery rate
786 (FDR) threshold < 0.4 were used for heatmap and volcano plot analyses, whereas genes with an
787 FDR threshold < 0.05 were used in gene ontology and pathway enrichment analysis.

788 **Gene ontology and pathway enrichment analyses**

789 Gene ontology (GO) and KEGG pathway enrichment analysis was conducted using Enrichr
790 (http://amp.pharm.mssm.edu/Enrichr) (Chen *et al.*, 2013; Kuleshov *et al.*, 2016). Genes with an
791 FDR threshold < 0.05 were analyzed with GO biological process 2018 and KEGG 2019 Mouse
792 databases. Full tables can be found in the supplementary material (Supplement_File_A).

793 **Classification of RNA-seq data**

794 Gene selection and normalization were performed using the R package DaMiRseq 1.2.0 (Chiesa,
795 Colombo and Piacentini, 2018). To distinguish TXN-fed samples from HFD control samples, we
796 used a correlation cutoff of 0.4 for the partial least-squares feature selection (FSelect), and the
797 default correlation coefficient for the redundant feature removal (FReduct).

798 **Cell culture**

799 Murine 3T3-L1 pre-adipocytes were obtained from ATCC (Rockville, MD, USA). Prior to
800 treatments, cells were maintained in basic media, which consisted of high glucose DMEM
801 supplemented with 1% penicillin-streptomycin and 10% heat-inactivated FBS (Hyclone, Logan,
802 UT, USA). The cells were allowed to reach full confluence for 2 days. Differentiation was
803 induced by the addition of 0.5 μM IBMX (Sigma-Aldrich, St. Louis, MO, USA), 0.25 μM
804 dexamethasone (Sigma-Aldrich) and 10 μg/ml insulin (Sigma-Aldrich) plus the addition of
805 treatment compounds XN or TXN. After 48 h, media was removed and fresh DMEM was
806 replenished for continuing differentiation. To observe XN and TXN's effects on 3T3-L1

807 adipocyte differentiation, different concentrations were selected based on dose-response
808 experiments to identify the dose that maximized effectiveness while minimizing cell toxicity.

809 **MTT cell viability assay**

810 For cell viability experiments using the MTT assay, 3T3-L1 fibroblasts were seeded in 96-well
811 plates at a density of 15,000 cells per well in 200 µl of DMEM medium supplemented with 10%
812 FBS, 1% glutamine, 1 mM of sodium pyruvate, 100 units/mL penicillin, and 100 µg/mL
813 streptomycin. After incubating 48 h with various concentrations of XN or TXN at 37°C in 5%
814 CO_2 atmosphere, the culture medium was removed and a solution of MTT [3-(4,5-
815 dimethylthiazol-2-yl)-2,5-diphenyltetrazolium bromide], 0.5 mg/mL in complete culture
816 medium, was added to each well. The cells were incubated with MTT for 3 h at 37°C and then
817 the MTT medium was removed before adding acidified isopropanol to each well. The cells were
818 shaken for 10 min in an orbital shaker before reading the absorbance at 570 nm using a
819 Microplate Reader (SpectraMax 190, Molecular Devices, Sunnyvale, CA, USA). Cell viability of
820 compound-treated cells was calculated as percent absorbance of vehicle-treated control cells.

821 **Oil red O staining**

822 Cells were washed twice with phosphate-buffer saline (PBS) and then fixed with 10% formalin
823 for 30 min. Cells were then washed with ddH_2O followed by 60% isopropanol. A 0.4% stock
824 solution of Oil Red O (Sigma-Aldrich) in isopropanol was diluted 3:2 (Oil red O:ddH_2O) for a
825 working solution. To determine intracellular lipid accumulation, fixed cells were incubated for
826 30 – 60 min at room temperature on a rocker with the Oil red O working solution. After
827 incubation, cells were washed with ddH_2O and imaged using microscopy.

828 **Adipocyte gene expression by RT-qPCR**

829 Total RNA was isolated as described above, dissolved in RNase-free water and stored at -80 ºC.
830 For RT-PCR experiments, cells were grown in 6-well plates and treated with XN and TXN at 25
831 µM concentration and differentiation medium after confluence for 2 days. Gene expression was
832 measured from cells at 7 d post treatment. RNA (0.25 µg) was converted to cDNA using iScript
833 reverse transcriptase and random hexamer primers (Bio-Rad Laboratories), according to the
834 manufacturer's recommendations. PCRs were set up as described previously (Gombart,
835 Borregaard and Koeffler, 2005). All the threshold cycle number (CT) were normalized to Ywhaz
836 reference gene. PrimeTime® Std qPCR assays were purchased from IDT (**Table 5**). ΔCT =

837 CT(target gene) – CT(reference gene). ΔΔCT = ΔCT(treated sample) – ΔCT(untreated sample/control
838 average). Statistics were done on ΔΔCT values.

839 Table 5 Primer probe information

Gene Name	IDT Assay Name	RefSeq Number
Cd36	Mm.PT.58.12375764	NM_007643
Cidec/Fsp27	Mm.PT.58.6462335	NM_178373
Fabp4	Mm.PT.58.43866459	NM_024406
Fgf21	Mm.PT.58.29365871.g	NM_020013
Il6	Mm.PT.58.10005566	NM_031168
Lpl	Mm.PT.58.46006099	NM_008509
Mogat1	Mm.PT.58.41635461	NM_026713
Pparγ2	Mm.PT.58.31161924	NM_011146
Ppargc1α	Mm.PT.58.28716430	NR_027710
Plin4	Mm.PT.58.43717773	NM_020568
Scd1	Mm.PT.58.8351960	NM_009127
Srebf1	Mm.PT.58.8508227	NM_011480

840 **Time-resolved fluorescence resonance energy transfer (TR-FRET)**

841 To determine the binding affinity of XN and TXN to PPARγ, a Lanthascreen™ TR-FRET
842 PPARγ competitive binding assay was performed by Thermo Fisher Scientific as described (cite
843 manual). A terbium-labeled anti-GST antibody binds to a GST-PPARγ-ligand binding domain
844 fusion protein in which the LBD is occupied by a fluorescent pan- PPAR ligand (Fluormone™
845 Pan-PPAR Green). Energy transfer from the antibody to the ligand occurs and a high TR-FRET
846 ratio (emission signal at 520 nm/495 nm) is detected. When a test compound displaces the ligand
847 from PPARγ-LBD, a decrease in the FRET signal occurs and a lower TR-FRET ratio is detected
848 (Invitrogen Corporation, 2008). A 10-point serial dilution (250,000 to 12.5 nM) of XN, TXN and
849 oleic acid was tested. Binding curves were generated by plotting percent displacement versus log
850 concentration (nM), and IC_{50} values were determined using a sigmoidal dose response (variable
851 slope).

852 **Molecular docking simulations for XN and TXN into the PPARγ ligand-binding domain**

853 To estimate the binding mode of XN and TXN to PPARγ, molecular docking simulations were
854 performed using AutoDock Vina (Trott and Olson, 2010). Structural models of XN and TXN
855 were built using OpenBabel to convert the isometric SMILES descriptor for XN to a PDB
856 formatted file, which was subsequently modified using PyMOL (The PyMOL Molecular

857 Graphics System, Version 1.7.4.5, Schrödinger, LLC) to obtain a PDB file for TXN. The solved
858 structure of PPARγ bound to the antagonist resveratrol (PDB ID: 4JAZ) was used as the receptor
859 model. The PDBQT files for the receptor and the resveratrol, XN, TXN, and oleic acid ligands
860 were generated using MGLTools-1.5.7rc1 (Morris *et al.*, 2009). The PPARγ receptor was kept
861 rigid during all docking experiments, and the center and size (20 x 20 x 20 $Å^3$) of the docking
862 box was positioned to cover the entire ligand-binding site of PPARγ. All rotatable torsion angles
863 in the ligand models were allowed to be active during the docking simulations. Twenty docking
864 poses were generated for each simulation, and the conformation with the lowest docking energy
865 was chosen as being representative.

866 **Statistical analysis**

867 Analysis of variance procedures for continuous data and Fisher's exact test for binary data were
868 used for statistical comparisons. P-values of orthogonal *a priori* comparisons of the HFD control
869 group versus each of the supplement groups are shown in the corresponding tables and figures.
870 Additional details of statistical analyses are described in the corresponding figure legends. Raw
871 data and scripts for all figures can be found on the github repository
872 (https://github.com/zhangyang2017/PPAR).

873 Author contributions

874 Conceptualization, Y.Z., G.B., C.L.M., J.F.S., C.S.M., and A.F.G.; Methodology, Y.Z., G.B.,
875 V.L.H., C.S.M., J.F.S., and A.F.G.; Investigation, Y.Z., M.B.L., C.L.M., C.P.W., C.V.L., V.L.H.
876 and A.F.G.; Formal analysis, Y.Z., G.B., C.V.L., V.L.H. and A.F.G.; Additional scientific
877 expertise and support, T.J.S., D.B.J.; C.V.L.; M.M.R. and M.B.L. Writing—original draft
878 preparation, Y.Z., G.B., V.L.H. and A.F.G.; Writing—review and editing, Y.Z., G.B., C.L.M.,
879 C.V.L., T.J.S., C.S.M., J.F.S., M.B.L. and A.F.G.; Visualization, Y.Z., G.B., D.B.J., V.L.H. and
880 A.F.G.; Resources, D.B.J., T.J.S., J.F.S., C.S.M. and A.F.G.; Funding acquisition, J.F.S., C.S.M.
881 and A.F.G. All authors have read and agreed to the published version of the manuscript.

882 Competing interests

883 The authors declare no competing interests, financial or non-financial, regarding this work. The
884 funders had no role in the design of the study; in the collection, analysis, or interpretation of
885 data; in the writing of the manuscript, or in the decision to publish the results.

Acknowledgements

We thank Jamie Pennington, Scott Leonard and Dr. Wenbin Wu for their assistance, Dr. Edward Davis for bioinformatics support and Anne-Marie Girard-Pohjanpelto, Mark Dasenko, Dr. Brent Kronmiller and Matthew Peterson at the Center of Genome Research and Bioinformatics at Oregon State University (OSU) for their assistance with RNA-sequencing. We thank Drs. Russ Turner and Urszula Iwaniec at the School of Biological and Population Health Sciences at OSU for use of the Lunar PIXImus 2 Dual Energy X-ray Absorptiometer (DXA) instrument.

Funding

The National Institutes of Health (NIH grants 5R01AT009168 to A.F.G., C.S.M., and J.F.S. and 1S10RR027878 to J.F.S.), the Linus Pauling Institute (LPI), the OSU College of Pharmacy, Hopsteiner, Inc., New York, and the OSU Foundation Buhler-Wang Research Fund supported this research. The Marion T. Tsefalas Graduate Fellowship from the LPI, the ZRT Laboratory Fund for the LPI, and the Charley Helen, Nutrition Science and Margy J. Woodburn Fellowships from the School of Biological and Population Health Sciences at OSU supported Y.Z.

900 **References**

901 Almeda-Valdés, P., Cuevas-Ramos, D. and Aguilar-Salinas, C. A. (2009) "Metabolic syndrome
902 and non-alcoholic fatty liver disease," *Annals of hepatology*, 8 Suppl 1, pp. S18-24.

903 Ammazzalorso, A. and Amoroso, R. (2019) "Inhibition of PPARγ by Natural Compounds as a
904 Promising Strategy in Obesity and Diabetes," *The open medicinal chemistry journal*, 13(1). doi:
905 10.2174/1874104501913010007.

906 Bechmann, L. P. *et al.* (2012) "The interaction of hepatic lipid and glucose metabolism in liver
907 diseases," *Journal of hepatology*, 56(4), pp. 952–964.

908 van Beek, L. *et al.* (2015) "The limited storage capacity of gonadal adipose tissue directs the
909 development of metabolic disorders in male C57Bl/6J mice," *Diabetologia*, 58(7), pp. 1601–
910 1609.

911 Bełtowski, J., Rachańczyk, J. and Włodarczyk, M. (2013) "Thiazolidinedione-induced fluid
912 retention: recent insights into the molecular mechanisms," *PPAR research*, 2013, p. 628628.

913 Bogue, M. A. *et al.* (2020) "Mouse Phenome Database: a data repository and analysis suite for
914 curated primary mouse phenotype data," *Nucleic acids research*, 48(D1), pp. D716–D723.

915 Brunt, E. M. and Tiniakos, D. G. (2010) "Histopathology of nonalcoholic fatty liver disease,"
916 *World journal of gastroenterology: WJG*, 16(42), pp. 5286–5296.

917 Brusotti, G. *et al.* (2017) "Betulinic acid is a PPARγ antagonist that improves glucose uptake,
918 promotes osteogenesis and inhibits adipogenesis," *Scientific reports*, 7(1), p. 5777.

919 Bugge, A. *et al.* (2010) "A novel intronic peroxisome proliferator-activated receptor gamma
920 enhancer in the uncoupling protein (UCP) 3 gene as a regulator of both UCP2 and -3 expression
921 in adipocytes," *The Journal of biological chemistry*, 285(23), pp. 17310–17317.

922 Bushnell, B. (2014) *BBMap: a fast, accurate, splice-aware aligner*. Lawrence Berkeley National
923 Lab.(LBNL), Berkeley, CA (United States). Available at:
924 https://www.osti.gov/servlets/purl/1241166.

925 Calleri, E. *et al.* (2014) "Resveratrol and its metabolites bind to PPARs," *Chembiochem: a*
926 *European journal of chemical biology*, 15(8), pp. 1154–1160.

927 Chao, L. *et al.* (2000) "Adipose tissue is required for the antidiabetic, but not for the
928 hypolipidemic, effect of thiazolidinediones," *The Journal of clinical investigation*, 106(10), pp.
929 1221–1228.

930 Chen, E. Y. *et al.* (2013) "Enrichr: interactive and collaborative HTML5 gene list enrichment
931 analysis tool," *BMC bioinformatics*, 14, p. 128.

932 Chen, Z. *et al.* (2012) "Insulin resistance and metabolic derangements in obese mice are
933 ameliorated by a novel peroxisome proliferator-activated receptor γ-sparing thiazolidinedione,"
934 *The Journal of biological chemistry*. ASBMB, 287(28), pp. 23537–23548.

935 Chiesa, M., Colombo, G. I. and Piacentini, L. (2018) "DaMiRseq-an R/Bioconductor package for
936 data mining of RNA-Seq data: normalization, feature selection and classification,"
937 *Bioinformatics* , 34(8), pp. 1416–1418.

938 Choi, S.-S. *et al.* (2016) "PPARγ Antagonist Gleevec Improves Insulin Sensitivity and Promotes
939 the Browning of White Adipose Tissue," *Diabetes*, 65(4), pp. 829–839.

940 Costa, R. *et al.* (2017) "Xanthohumol and 8-prenylnaringenin ameliorate diabetic-related
941 metabolic dysfunctions in mice," *The Journal of nutritional biochemistry*, 45, pp. 39–47.

942 Dobin, A. *et al.* (2013) "STAR: ultrafast universal RNA-seq aligner," *Bioinformatics* , 29(1), pp.
943 15–21.

944 Dorn, C. *et al.* (2010) "Xanthohumol, a chalcon derived from hops, inhibits hepatic inflammation
945 and fibrosis," *Molecular nutrition & food research*, 54 Suppl 2, pp. S205-13.

946 Estes, C. *et al.* (2018) "Modeling the epidemic of nonalcoholic fatty liver disease demonstrates
947 an exponential increase in burden of disease," *Hepatology* , 67(1), pp. 123–133.

948 Fang, L. *et al.* (2016) "PPARgene: A Database of Experimentally Verified and Computationally
949 Predicted PPAR Target Genes," *PPAR research*, 2016, p. 6042162.

950 Fonseca, V. (2003) "Effect of thiazolidinediones on body weight in patients with diabetes
951 mellitus," *The American journal of medicine*, 115 Suppl 8A, pp. 42S-48S.

952 Frankish, A. *et al.* (2019) "GENCODE reference annotation for the human and mouse genomes,"
953 *Nucleic acids research*, 47(D1), pp. D766–D773.

954 Garcia-Jaramillo, M. *et al.* (2019) "Lipidomic and transcriptomic analysis of western diet-
955 induced nonalcoholic steatohepatitis (NASH) in female Ldlr -/- mice," *PloS one*, 14(4), p.
956 e0214387.

957 Goldberg, I. J. and Ginsberg, H. N. (2006) "Ins and outs modulating hepatic triglyceride and
958 development of nonalcoholic fatty liver disease," *Gastroenterology*, 130(4), pp. 1343–1346.

959 Gombart, A. F., Borregaard, N. and Koeffler, H. P. (2005) "Human cathelicidin antimicrobial
960 peptide (CAMP) gene is a direct target of the vitamin D receptor and is strongly up-regulated in
961 myeloid cells by 1, 25-dihydroxyvitamin D3," *The FASEB journal*. FASEB, 19(9), pp. 1067–
962 1077.

963 Gong, Z. *et al.* (2009) "The role of tanshinone IIA in the treatment of obesity through
964 peroxisome proliferator-activated receptor gamma antagonism," *Endocrinology*, 150(1), pp.
965 104–113.

966 Goto, T. *et al.* (2013) "Natural compounds regulate energy metabolism by the modulating the
967 activity of lipid-sensing nuclear receptors," *Molecular nutrition & food research*. Wiley Online
968 Library, 57(1), pp. 20–33.

969 Griffin, J. D. *et al.* (2017) "Role of Hepatic PLIN2 and PLIN4 in The Development of Western
970 Type Diet Induced Hepatosteatosis," *The FASEB Journal*. John Wiley & Sons, Ltd, 31(S1), pp.
971 458.3-458.3.

972 Hashimoto, E., Taniai, M. and Tokushige, K. (2013) "Characteristics and diagnosis of
973 NAFLD/NASH," *Journal of gastroenterology and hepatology*, 28 Suppl 4, pp. 64–70.

974 Henney, J. E. (2000) "Withdrawal of Troglitazone and Cisapride," *JAMA: the journal of the*
975 *American Medical Association*. American Medical Association, 283(17), pp. 2228–2228.

976 Invitrogen Corporation (2008) *LanthaScreen™ TR-FRET PPARg Assay Manual*. Carlsbad, CA,
977 USA. Available at:
978 https://www.thermofisher.com/order/catalog/product/PV4894?us&en#/PV4894?us&en.

979 Ipsen, D. H., Lykkesfeldt, J. and Tveden-Nyborg, P. (2018) "Molecular mechanisms of hepatic
980 lipid accumulation in non-alcoholic fatty liver disease," *Cellular and molecular life sciences:*
981 *CMLS*, 75(18), pp. 3313–3327.

982 Jia, Y. *et al.* (2012) "The natural carotenoid astaxanthin, a PPAR-α agonist and PPAR-γ
983 antagonist, reduces hepatic lipid accumulation by rewiring the transcriptome in lipid-loaded
984 hepatocytes," *Molecular nutrition & food research*, 56(6), pp. 878–888.

985 Karbowska, J. and Kochan, Z. (2012) "Intermittent fasting up-regulates Fsp27/Cidec gene
986 expression in white adipose tissue," *Nutrition* , 28(3), pp. 294–299.

987 Kim, S.-J., Nian, C. and McIntosh, C. H. S. (2011) "Adipocyte expression of the glucose-
988 dependent insulinotropic polypeptide receptor involves gene regulation by PPARγ and histone
989 acetylation," *Journal of lipid research*, 52(4), pp. 759–770.

990 Kim, Y.-J. *et al.* (2008) "Transcriptional activation of Cidec by PPARgamma2 in adipocyte,"
991 *Biochemical and biophysical research communications*, 377(1), pp. 297–302.

992 Kirkwood, J. S. *et al.* (2013) "A metabolomics-driven elucidation of the anti-obesity mechanisms
993 of xanthohumol," *The Journal of biological chemistry*, 288(26), pp. 19000–19013.

994 Kuleshov, M. V. *et al.* (2016) "Enrichr: a comprehensive gene set enrichment analysis web
995 server 2016 update," *Nucleic acids research*, 44(W1), pp. W90-7.

996 Kwak, H. J. *et al.* (2016) "Suppression of Adipocyte Differentiation by Foenumoside B from
997 Lysimachia foenum-graecum Is Mediated by PPARγ Antagonism," *PloS one*, 11(5), p.
998 e0155432.

999 Lawrence, M. *et al.* (2013) "Software for computing and annotating genomic ranges," *PLoS*
1000 *computational biology*, 9(8), p. e1003118.

1001 Lee, J.-E. and Ge, K. (2014) "Transcriptional and epigenetic regulation of PPARγ expression
1002 during adipogenesis," *Cell & bioscience*, 4, p. 29.

1003 Lee, Y. J. *et al.* (2012) "Nuclear receptor PPARγ-regulated monoacylglycerol O-acyltransferase
1004 1 (MGAT1) expression is responsible for the lipid accumulation in diet-induced hepatic
1005 steatosis," *Proceedings of the National Academy of Sciences of the United States of America*,
1006 109(34), pp. 13656–13661.

1007 Lefterova, M. I. *et al.* (2014) "PPARγ and the global map of adipogenesis and beyond," *Trends*
1008 *in endocrinology and metabolism: TEM*, 25(6), pp. 293–302.

1009 Legette, L. *et al.* (2014) "Human pharmacokinetics of xanthohumol, an antihyperglycemic
1010 flavonoid from hops," *Molecular nutrition & food research*, 58(2), pp. 248–255.

1011 Lehmann, J. M. *et al.* (1995) "An Antidiabetic Thiazolidinedione Is a High Affinity Ligand for
1012 Peroxisome Proliferator-activated Receptor γ (PPARγ)," *The Journal of biological chemistry*,
1013 270(22), pp. 12953–12956.

1014 Li, Y.-T. *et al.* (2009) "7-Chloroarctinone-b as a new selective PPARgamma antagonist potently
1015 blocks adipocyte differentiation," *Acta pharmacologica Sinica*, 30(9), pp. 1351–1358.

1016 Lighton, J. R. B. and Halsey, L. G. (2011) "Flow-through respirometry applied to chamber
1017 systems: pros and cons, hints and tips," *Comparative biochemistry and physiology. Part A,*
1018 *Molecular & integrative physiology*, 158(3), pp. 265–275.

1019 Lytle, K. A., Wong, C. P. and Jump, D. B. (2017) "Docosahexaenoic acid blocks progression of
1020 western diet-induced nonalcoholic steatohepatitis in obese Ldlr-/- mice," *PloS one*, 12(4), p.
1021 e0173376.

1022 Mahli, A. *et al.* (2019) "Therapeutic Application of Micellar Solubilized Xanthohumol in a
1023 Western-Type Diet-Induced Mouse Model of Obesity, Diabetes and Non-Alcoholic Fatty Liver
1024 Disease," *Cells* , 8(4). doi: 10.3390/cells8040359.

1025 Matsusue, K. *et al.* (2003) "Liver-specific disruption of PPARgamma in leptin-deficient mice
1026 improves fatty liver but aggravates diabetic phenotypes," *The Journal of clinical investigation*,
1027 111(5), pp. 737–747.

1028 Matsusue, K. *et al.* (2008) "Hepatic steatosis in leptin-deficient mice is promoted by the
1029 PPARgamma target gene Fsp27," *Cell metabolism*, 7(4), pp. 302–311.

1030 Medvedev, A. V. *et al.* (2001) "Transcriptional regulation of the mouse uncoupling protein-2
1031 gene. Double E-box motif is required for peroxisome proliferator-activated receptor-gamma-
1032 dependent activation," *The Journal of biological chemistry*, 276(14), pp. 10817–10823.

1033 Mendes, V. *et al.* (2008) "Xanthohumol influences preadipocyte differentiation: implication of
1034 antiproliferative and apoptotic effects," *Journal of agricultural and food chemistry*, 56(24), pp.
1035 11631–11637.

1036 Miranda, C. L. *et al.* (2016) "Xanthohumol improves dysfunctional glucose and lipid metabolism
1037 in diet-induced obese C57BL/6J mice," *Archives of biochemistry and biophysics*, 599, pp. 22–30.

1038 Miranda, C. L. *et al.* (2018) "Non-estrogenic Xanthohumol Derivatives Mitigate Insulin
1039 Resistance and Cognitive Impairment in High-Fat Diet-induced Obese Mice," *Scientific reports*,
1040 8(1), p. 613.

1041 Miyata, S. *et al.* (2015) "Xanthohumol Improves Diet-induced Obesity and Fatty Liver by
1042 Suppressing Sterol Regulatory Element-binding Protein (SREBP) Activation," *The Journal of*
1043 *biological chemistry*, 290(33), pp. 20565–20579.

1044 Morris, G. M. *et al.* (2009) "AutoDock4 and AutoDockTools4: Automated docking with
1045 selective receptor flexibility," *Journal of computational chemistry*, 30(16), pp. 2785–2791.

1046 Nesto, R. W. *et al.* (2004) "Thiazolidinedione use, fluid retention, and congestive heart failure: a
1047 consensus statement from the American Heart Association and American Diabetes Association,"
1048 *Diabetes care*, 27(1), pp. 256–263.

1049 Park, S. Y. *et al.* (2008) "Cilostazol increases 3T3-L1 preadipocyte differentiation with improved
1050 glucose uptake associated with activation of peroxisome proliferator-activated receptor-γ
1051 transcription," *Atherosclerosis*, 201(2), pp. 258–265.

1052 Promrat, K. *et al.* (2004) "A pilot study of pioglitazone treatment for nonalcoholic
1053 steatohepatitis," *Hepatology* , 39(1), pp. 188–196.

1054 Ratziu, V. *et al.* (2008) "Rosiglitazone for nonalcoholic steatohepatitis: one-year results of the
1055 randomized placebo-controlled Fatty Liver Improvement with Rosiglitazone Therapy (FLIRT)
1056 Trial," *Gastroenterology*, 135(1), pp. 100–110.

1057 Ratziu, V. *et al.* (2010) "Long-term efficacy of rosiglitazone in nonalcoholic steatohepatitis:
1058 results of the fatty liver improvement by rosiglitazone therapy (FLIRT 2) extension trial,"
1059 *Hepatology* , 51(2), pp. 445–453.

1060 Rayalam, S. *et al.* (2009) "Anti-obesity effects of xanthohumol plus guggulsterone in 3T3-L1
1061 adipocytes," *Journal of medicinal food*, 12(4), pp. 846–853.

1062 Robinson, M. D., McCarthy, D. J. and Smyth, G. K. (2010) "edgeR: a Bioconductor package for
1063 differential expression analysis of digital gene expression data," *Bioinformatics* , 26(1), pp. 139–
1064 140.

1065 Robinson, M. D. and Oshlack, A. (2010) "A scaling normalization method for differential
1066 expression analysis of RNA-seq data," *Genome biology*, 11(3), p. R25.

1067 Rosen, E. D. and Spiegelman, B. M. (2006) "Adipocytes as regulators of energy balance and
1068 glucose homeostasis," *Nature*, 444(7121), pp. 847–853.

1069 Samuels, J. S., Shashidharamurthy, R. and Rayalam, S. (2018) "Novel anti-obesity effects of
1070 beer hops compound xanthohumol: role of AMPK signaling pathway," *Nutrition & metabolism*,
1071 15, p. 42.

1072 Sankella, S., Garg, A. and Agarwal, A. K. (2016) "Characterization of the Mouse and Human
1073 Monoacylglycerol O-Acyltransferase 1 (Mogat1) Promoter in Human Kidney Proximal Tubule
1074 and Rat Liver Cells," *PloS one*, 11(9), p. e0162504.

1075 Sanyal, A. J. *et al.* (2010) "Pioglitazone, vitamin E, or placebo for nonalcoholic steatohepatitis,"
1076 *The New England journal of medicine*, 362(18), pp. 1675–1685.

1077 Schwartz, A. V. (2008) "TZDs and Bone: A Review of the Recent Clinical Evidence," *PPAR*
1078 *research*, 2008, p. 297893.

1079 Schwartz, A. V. and Sellmeyer, D. E. (2007) "Thiazolidinediones: new evidence of bone loss,"
1080 *The Journal of clinical endocrinology and metabolism*, pp. 1232–1234.

1081 Sharma, A. M. and Staels, B. (2007) "Review: Peroxisome proliferator-activated receptor
1082 gamma and adipose tissue--understanding obesity-related changes in regulation of lipid and
1083 glucose metabolism," *The Journal of clinical endocrinology and metabolism*, 92(2), pp. 386–
1084 395.

1085 Soccio, R. E., Chen, E. R. and Lazar, M. A. (2014) "Thiazolidinediones and the promise of
1086 insulin sensitization in type 2 diabetes," *Cell metabolism*, 20(4), pp. 573–591.

1087 Speakman, J. R. (2013) "Measuring energy metabolism in the mouse - theoretical, practical, and
1088 analytical considerations," *Frontiers in physiology*, 4, p. 34.

1089 Stefan, N., Häring, H.-U. and Cusi, K. (2019) "Non-alcoholic fatty liver disease: causes,
1090 diagnosis, cardiometabolic consequences, and treatment strategies," *The lancet. Diabetes &*
1091 *endocrinology*, 7(4), pp. 313–324.

1092 Strathmann, J. and Gerhauser, C. (2012) "Anti-proliferative and Apoptosis-Inducing Properties
1093 of Xanthohumol, a Prenylated Chalcone from Hops (Humulus lupulus L.)," in Diederich, M. and
1094 Noworyta, K. (eds.) *Natural compounds as inducers of cell death: volume 1*. Dordrecht: Springer
1095 Netherlands, pp. 69–93.

1096 Takahashi, K. and Osada, K. (2017) "Effect of Dietary Purified Xanthohumol from Hop
1097 (Humulus lupulus L.) Pomace on Adipose Tissue Mass, Fasting Blood Glucose Level, and Lipid
1098 Metabolism in KK-Ay Mice," *Journal of oleo science*, 66(5), pp. 531–541.

1099 Tamori, Y. *et al.* (2002) "Role of peroxisome proliferator-activated receptor-gamma in
1100 maintenance of the characteristics of mature 3T3-L1 adipocytes," *Diabetes*, 51(7), pp. 2045–
1101 2055.

1102 Team, B. C. (2016) "Mus. musculus: Annotation package for the Mus. musculus object," *R*
1103 *package version*, 1(1).

1104 Trott, O. and Olson, A. J. (2010) "AutoDock Vina: improving the speed and accuracy of docking
1105 with a new scoring function, efficient optimization, and multithreading," *Journal of*
1106 *computational chemistry*, 31(2), pp. 455–461.

1107 Tschöp, M. H. *et al.* (2011) "A guide to analysis of mouse energy metabolism," *Nature methods*,
1108 9(1), pp. 57–63.

1109 Wahlström, A. *et al.* (2016) "Intestinal Crosstalk between Bile Acids and Microbiota and Its
1110 Impact on Host Metabolism," *Cell metabolism*, 24(1), pp. 41–50.

1111 Weir, J. B. D. E. B. (1949) "New methods for calculating metabolic rate with special reference to
1112 protein metabolism," *The Journal of physiology*, 109(1–2), pp. 1–9.

1113 Wolf Greenstein, A. *et al.* (2017) "Hepatocyte-specific, PPARγ-regulated mechanisms to
1114 promote steatosis in adult mice," *The Journal of endocrinology*, 232(1), pp. 107–121.

1115 Yang, J.-Y. *et al.* (2007) "Effect of xanthohumol and isoxanthohumol on 3T3-L1 cell apoptosis
1116 and adipogenesis," *Apoptosis: an international journal on programmed cell death*, 12(11), pp.
1117 1953–1963.

1118 Yang, T. and Soodvilai, S. (2008) "Renal and vascular mechanisms of thiazolidinedione-induced
1119 fluid retention," *PPAR research*, 2008, p. 943614.

1120 Younossi, Z. M. *et al.* (2016) "Global epidemiology of nonalcoholic fatty liver disease-Meta-
1121 analytic assessment of prevalence, incidence, and outcomes," *Hepatology* , 64(1), pp. 73–84.

1122 Yui, K., Kiyofuji, A. and Osada, K. (2014) "Effects of xanthohumol-rich extract from the hop on
1123 fatty acid metabolism in rats fed a high-fat diet," *Journal of oleo science*, 63(2), pp. 159–168.

1124 Zhang, Y. *et al.* (2014) "Protopanaxatriol, a novel PPARγ antagonist from Panax ginseng,
1125 alleviates steatosis in mice," *Scientific reports*, 4, p. 7375.

1126 Zhang, Y. *et al.* (2016) "Dietary component isorhamnetin is a PPARγ antagonist and ameliorates
1127 metabolic disorders induced by diet or leptin deficiency," *Scientific reports*, 6, p. 19288.

1128 Zhang, Y. *et al.* (2020) "Improvements in Metabolic Syndrome by Xanthohumol Derivatives Are
1129 Linked to Altered Gut Microbiota and Bile Acid Metabolism," *Molecular nutrition & food*
1130 *research*, 64(1), p. e1900789.

1131 Zhu, Y. *et al.* (1993) "Cloning of a new member of the peroxisome proliferator-activated
1132 receptor gene family from mouse liver," *The Journal of biological chemistry*, 268(36), pp.
1133 26817–26820.